Muon spin spectroscopy

Adrian D. Hillier[1*], Stephen J Blundell[2], Iain McKenzie[3, 4, 5], Izumi Umegaki[6], Lei Shu[7], Joseph A. Wright[8], Thomas Prokscha[9], Fabrice Bert[10], Koichiro Shimomura[11], Adam Berlie[1], Helena Alberto[12], and Isao Watanabe[13]

1 ISIS Neutron and Muon facility, STFC Rutherford Appleton Laboratory, Didcot, Oxford, United Kingdom

2 Clarendon Laboratory, Department of Physics, University of Oxford, Oxford, United Kingdom

3 TRIUMF, Vancouver, BC, Canada,

4 Department of Chemistry, Simon Fraser University, Burnaby, BC, Canada

5 Department of Physics and Astronomy, University of Waterloo, Waterloo, ON, Canada

6 Toyota Central R&D Labs., Inc., Nagakute, Aichi, Japan

7 State Key Laboratory of Surface Physics and Department of Physics, Fudan University, Shanghai, China

8 School of Chemistry, University of East Anglia, Norwich, United Kingdom

9 Laboratory for Muon Spin Spectroscopy, Paul Scherrer Institute, Villigen PSI, Switzerland

10 Université Paris-Saclay, CNRS, Laboratoire de Physique des Solides, Orsay, France

11 High Energy Accelerator Research Organization (KEK), Tsukuba, Ibaraki, Japan

12 University of Coimbra, CFisUC, Department of Physics, R. Larga, Coimbra, Portugal

13 Advanced Meson Science Laboratory, RIKEN, Wako, Saitama , Japan

*Corresponding Author: adrian.hillier@stfc.ac.uk

Abstract

Muons are spin-½ particles that can be implanted into a wide range of condensed matter materials to act as a local probe of the surrounding atomic environment. By measuring the interaction of the muon with its local environment via its precession and relaxation, unique information about the static and dynamic magnetic or atomic effects in the material of interest, can be obtained. This has enabled muon spin spectroscopy or muon spin rotation / relaxation / resonance (μSR) to develop into a powerful tool to investigate the properties of materials such as fundamental magnetism, superconductivity (and its interplay with magnetism), functional materials, energy storage materials including ionic diffusion in potential battery materials, the dynamics of soft matter, free radical chemistry, reaction kinetics, semiconductors, advanced manufacturing and cultural artefacts. This Primer is intended as an introductory article and introduces the μSR technique, the typical types of results obtainable with the

technique, and some recent science advances across various fields. We also discuss data reproducibility and limitations issues before highlighting promising future developments for the technique.

[H1] Introduction

The muon μ is a fundamental particle similar to the electron (electric charge $-e$ and a spin of ½) but with greater mass (see Table 1 for muon properties). Both the mass and gyromagnetic ratio **[G]** of the muon are between those of the electron and the proton: in materials, the negative muon μ^- behaves like a heavy electron and its antiparticle; the positive muon μ^+, like a light proton. The discovery of the muon is generally attributed to Anderson and Neddermeyer[1] while the history of muon spin spectroscopy can be traced back to a seminal paper by Garwin et al[2] and subsequent investigations by a Jesuit priest[3], some adventurous balloon travel[4] and the measurement of the muon lifetime in Rome[5].

Most muon spectroscopy studies of condensed matter use the positive muon μ^+, mainly due to the increased production rates and because, during the implantation into the sample, the polarisation is maintained compared to the negative muon, due to spin-orbit coupling.

A critical advantage of using muons is that the experiment can be conducted in zero field, as the muon is spin polarised at source, and that it does not require a specific element in the sample. Unlike many other techniques, such as neutron scattering/spectroscopy and X-rays, muons are implanted into the sample and can be seen as analogous to NMR and EPR since the depolarisation of a spin polarised [G] species is measured. Although, X-ray absorption spectroscopy can be used to study magnetic atoms to gain insight into the spin and orbital angular momentums, however, this is not a temporal technique, and the muon is a much more sensitive probe to weak magnetism, for example if you have diffuse moments such as that observed in short range order or organic based systems. Neutron spectroscopy can be used to study a wide range of matter from both hard to soft matter and in areas ranging from magnetism, ionic diffusion, liquid interfaces, lattice vibrations, however, the time-window is different and neutron spectroscopy is less sensitive to weak electronic and nuclear moments when compared to muon techniques. When positive or negative muons are implanted into a sample, they will interact with their local environment before decaying into a positron or electron for μ^+ or μ^- respectively, preferentially along or opposite the final spin direction. By monitoring the spin polarisation, information about the material of interest can be obtained. The positively charged muon implants between the nuclei, making it sensitive to the physics of the electrons, while the negatively charged muon implants close to the atomic nucleus, and can yield information about the identity of the capturing atom and local magnetism (see the science example later).

	electron	muon	proton
Charge	- e	+/- e	+ e
Spin	1/2	1/2	1/2
Mass (m_e)	1	207 m_e (or 0.11 m_p)	1836
Lifetime, τ_μ	∞	μ^+: 2.197 μs μ^-: dependent on capturing atom < 2.197 μs	∞
Magnetic Moment, (m_p)	657	3.18	1
Gyromagnetic ratio, γ/2π (MHz/T)	2.8×10^4	135.5	42.6

Table 1: Properties of the muon, electron and proton

In order to produce polarised muons in significant quantities, a proton accelerator is required. These large facilities are often expensive to build and operate, and hence they are user facilities that scientists visit. There are currently five sources that produce muons useful for investigating materials, namely (in chronological order) TRIUMF (Canada), PSI (Switzerland), ISIS (UK), J-PARC (Japan) and MuSIC (Japan). These are well-established user facilities that have a range of instruments that have been optimised for investigating the broad range of science where muon spectroscopy is of value. The basic instrument consists of a source of muons which are transported to the instrument. Upon arrival at the instrument, a trigger signal activates the data acquisition system and the muons enter the material of interest. After which the muons will interact with the local environment and decay, emitting a positron (μ^+), or an electron (μ^-), and in the case of the negative muon, muonic X-ray and γ-ray (μ^-) are emitted during the capture process. The material of interest may be inside a piece of equipment that may control temperature, and/or magnetic field, and/or pressure and/or other factors. Around the material are detectors that time stamp any emission. From these detectors, the time evolution of the muon in the material can be determined. The experimental setups are normally defined by the applied magnetic field. These are usually zero-field, longitudinal field and transverse field, relative to the initial muon polarisation. During a typical muon experiment, an ensemble average of the muon depolarisation is measured, the muon lifetime is removed and the asymmetry of the depolarisation is recorded. It is often this depolarisation that is of interest and although statistics vary on the level of detail required, typically several million events are counted per data point e.g. temperature.

This article is intended as an introduction to the subject of muon spin spectroscopy for condensed matter and while each section can be read in isolation, however it is easier to read sequentially

through the Primer. 'Experimentation' explains details of the technique and experimental acquisition; 'Results' discusses how to treat the acquired data and analyse the results; 'Applications' reports on current topics using μSR; 'Reproducibility and Data Deposition' discusses the data storage at facilities and calibration values for ensuring the data can be reproduced; 'Limitations and Optimisations' provides an overview of some of the practical elements for a successful muon experiment. Finally, 'Outlook', we cover some new trends and developments. While we provide an overview of the μSR technique, more information and a number of more specialised and detailed books and articles are available to the reader[6-13].

BOX 1: Comparison of Muon Sources

There are two types of muon sources: continuous sources and pulsed muon sources, with each having their own strengths and limitations. TRIUMF, PSI and MuSIC are continuous muon sources which have high timing resolution whereas ISIS and J-PARC are pulsed sources which have high data rates and can measure out to 'long' times. In addition to the intrinsic muon source characteristics, each facility has a range of beamlines. Table 2 summarises the characteristics of each source. The details of each type of beamline is discussed in the experimentation section.

Facility	Type of beamline	Momentum (Mev/c)
TRIUMF	Surface	29.5 +/- 10%
	Decay	40 - 120
PSI	Low Energy Muons	0.45 – 2.5
	Surface	28
	Decay	60 - 125
ISIS	Surface	29
	Decay	15-120
J-PARC	Low Energy Muons (in development)	
	Surface	30
	Decay	5 - 120
MuSIC	Surface	28
	Decay	28 - 80

Table 2: A summary of the facilities and the different beamlines that are available. The technical details of the different muon beamlines are described in the experimentation section.

[H1] Experimentation

In this section, we give an overview of instrument design and provide the user with some fundamental knowledge about muon experimentation. While understanding the instrumentation should help with assessing how suitable μSR is to investigate specific systems and with writing research proposals for access to beamtime, typically every facility will have instrument scientists who will guide and support users through the experimental setup and the data acquisition process.

[H2] Muon production, sources and beamlines

Producing muons in a great enough quantity to perform experiments is achieved by the collision of protons p with a target made of light elements such as carbon or beryllium, which results in pions π **[G]** that decay into muons. This process is summarised below, where n represents neutrons:

$$p + p \rightarrow p + n + \pi^+ \qquad \text{(Eq. 1)}$$
$$p + n \rightarrow p + p + \pi^- \qquad \text{(Eq. 2)}$$

Because current facilities have proton energies between 500 MeV and 3 GeV, this high-energy collision process creates both negatively and positively charged pions. The decay of pions results in muons and muon neutrinos ν_μ [***G***] , where

$$\pi^+ \rightarrow \mu^+ + \nu_\mu \qquad \text{(Eq.3)}$$
$$\pi^- \rightarrow \mu^- + \bar{\nu}_\mu \qquad \text{(Eq. 4)}$$

Because the spin of the pion is zero and the muon neutrino has a definite helicity **[G]**, the surface muons produced are 100% spin-polarised **[G]**, whereas decay muons, produced from in-flight pion decay have lower polarisation.

These muons decay, emitting a positron e^+ (or electron e^-) and two neutrinos ν. The positron is emitted preferentially along the direction of the muon spin.

$$\mu^+ \rightarrow e^+ + \bar{\nu}_\mu + \nu_e \qquad \text{(Eq. 5)}$$
$$\mu^- \rightarrow e^- + \nu_\mu + \bar{\nu}_e \qquad \text{(Eq. 6)}$$

Large-scale user facilities can provide two types of muon beam lines: surface and decay muons.

Surface muons originate from decay of the pions at rest at the surface of the target material. They have a relatively low energy (~4MeV) and momentum (~28 MeV/c) with a fairly narrow energy distribution, and most importantly, 100 % spin polarisation. The yield is also fairly high (only a small fraction of the pions or muons can be collected and transported to experimental areas), but with a large number of polluting positrons and other particles that must be removed before the muons reach the sample. The surface method is used for the production of μ^+ because most of the stopped negative pions undergo nuclear capture **[G]** before they decay, and therefore almost no surface negative muons escape from the target. However, the large amount of μ^+ produced provides a high flux of muons for μSR experiments.

In decay muon beam lines, high-energy pions are ejected from the target and transported down a beam line so that pion decay occurs in flight, generally when the pions are contained in a superconducting solenoid whose length is comparable to the pion decay length. Typical momenta for these beam lines range from 40 to 120 MeV/c and is tuned by varying the dipole magnetic fields. An example of this is shown in **Error! Reference source not found.**, where Figure 1a shows the RIKEN-RAL facilities at ISIS[14,15]. This allows for the production of high-energy muons (important for pressure cell work and other experiments in which higher muon penetration depths are required) and negative muons (negative pion extraction from the target is required). The production rates for these higher energy muons is generally lower than surface energy muons, particularly just above the surface energy and slowly recovers as the momentum is increased (see **Error! Reference source not found.**b).

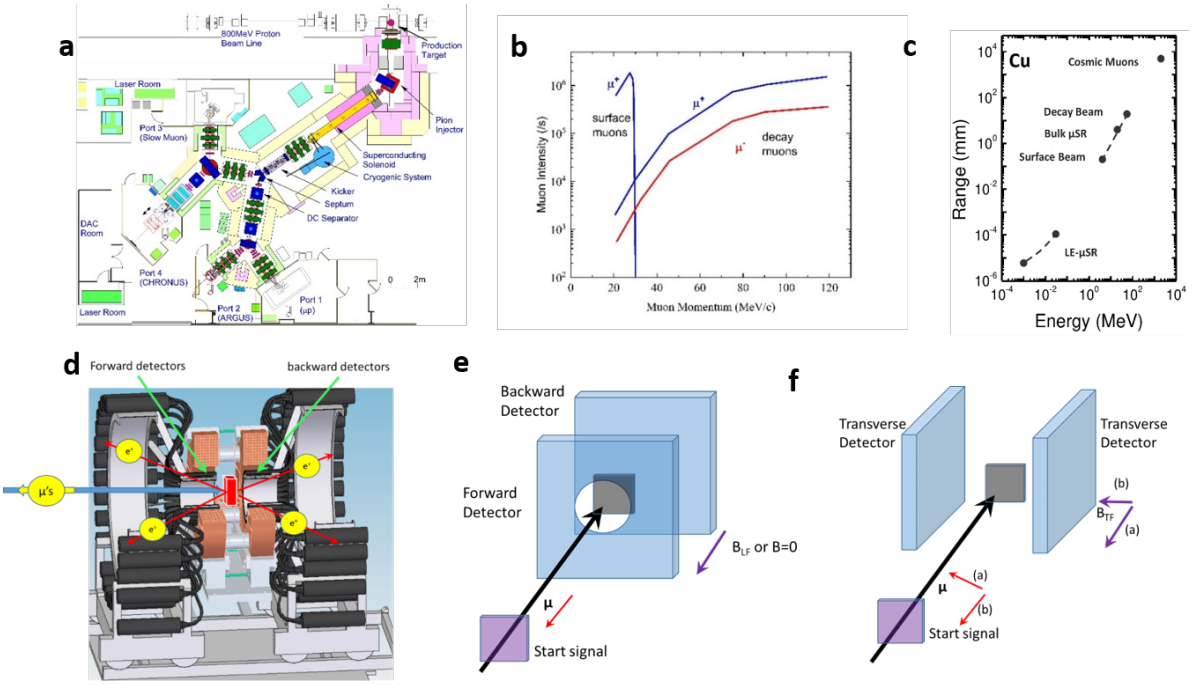

Figure 1: (a) A schematic of a decay muon beamline. This is the layout of the RIKEN-RAL beamline at ISIS and (b) the muon production rate for RIKEN-RAL. c) Range of muons in Cu as a function of muon energy. d) a schematic diagram of a μSR spectrometer. The number of positrons generated by the decay of muons at rest in a sample (red) are measured using counters placed in front and behind (black segments coming from close to the sample, scintillators, to the black tubes, photo multiplier tubes. The beige segment is a Helmholtz coil for producing magnetic fields. e-f) A schematic of a typical muon spin spectrometer in both the longitudinal setup (e) and the transverse setup (f). The transverse setup has two configurations a or b and is instrument dependent. The detectors are coloured pale blue and the start detector in pale purple. The start detector may be a muon detector (continuous) or a signal from the accelerator (pulsed). The muon spin is represented by the red arrows and the field direction by the purple arrows.

The proton source generally comes from two different set-ups, a cyclotron **[G]** or a synchrotron **[G],** which are quasi-continuous (23 – 50 MHz) or pulsed (25 – 50 Hz) respectively.

A quasi-continuous source uses a cyclotron (PSI, Switzerland[16], TRIUMF, Canada[17] and MuSIC, Japan[18]), and generates an extremely high flux of muons, of the order of 10^8 $mA^{-1}s^{-1}$. One of the main advantages of a continuous source is that the time resolution **[G]** can be extremely high, and one can measure large frequencies up to, and perhaps beyond, 5 GHz. This enables high muon precession frequencies to be measured, such as those arising from internal fields in magnetic samples and in muonium studies. However, the rate for time differential measurements is limited by only being able to have one muon in the sample at a time, counting approximately 20 million muons per hour.

For a pulsed source (ISIS, UK[15] and J-PARC, Japan[19]), a synchrotron is used to create a pulse of protons with a finite pulse width that collides with a target. The muons produced from the collision travel in bunches with a finite pulse width (at ISIS, this pulse width is approximately 100 ns [20] and at J-PARC the pulse width is 100 ns). As the front of the pulse arrives first, these first muons will thermalise **[G]** and begin to precess **[G]** or respond to any local fields before the rest of the muon ensemble arrive. The result of this pulse width is that the time resolution is significantly limited with measurable frequencies up to ~10 MHz. The advantage of the pulse structure is that one has periods of "quiet" between the pulses, which means the background of the measurement is low and one can record positrons for many muon lifetimes (>12 τ_μ, 26 μs). Pulsed measurements lead to very high instantaneous data rates (i.e. positron detected in the detector system) that require large arrays of positron detectors to cope. This leads to the need to build extensive beam lines and instruments such as those seen at ISIS [15,21] and J-PARC[19]. Another advantage of pulsed muons is the ease with which they can be combined with pulsed extreme conditions such as lasers, pulsed RF field, pulsed E-Field, pulsed current, in-situ battery decay and in principle pulsed high magnetic fields. This enables both stimulation of the sample and measurements of the physical effects of this with muons. For time-integral measurements **[G]** there is no restriction on the number of muons in the sample at one time, so it is possible to run at a much higher incident muon rate at a continuous source, far greater than a pulsed source. At pulsed source facilities, time-differential **[G]** and time-integral measurements can be performed simultaneously, while an advantage of continuous source facilities is the much higher data rates for time-integral measurements. This higher data rate allows for more sensitive measurements. Depending on the science and the information needed, either time-differential or time-integral measurements are optimal. The science examples discussed later will indicate which technique, and source, is best.

Beamlines are used to transport muons from the target to the sample, the muon then decays and the resulting product is detected. Because muons have both charge and spin, various magnets guide and steer the beam from injection from the target to individual instruments (**Error! Reference source not found.**a). Quadrupole magnets **[G]** are used to focus the muon beam, where each quadrupole is responsible for focusing along either the x or y axes and they act together as a series of lenses. When using only quadrupoles, other particles are also transported down the beam line; one can selectively remove these other particles by using dipole bending magnets, which also serve to curve the beam to meet the spatial requirements of the beam line. Momentum slits **[G]** can filter out all particles that do not have the same momentum and charge as the muon, while a separator **[G]** also filters out positron contamination (where positrons have the same momentum as the muons but different velocities) by only letting muons of the desired velocity through. At a pulse source, the proton pulses arrive in two bunches close together (at ISIS ~300 ns apart). Having both pulses enter a single muon instrument can be detrimental to the frequency response and so to make the most of the two pulses, the muon beam can be kicked **[G]** to different individual beam lines, thus enabling two instruments to operate simultaneously. 'Kickers' have also been used at continuous sources to reduce the detector

background, giving the instruments a muon on request option[22]. Although bending the path of a muon may also cause a slight rotation to its spin, larger rotations can be achieved by using magnetic fields where the spin of the muon can be rotated between 70° to 90° and an electric cross field ensures the muons do not deviate from the beamline. This enables high transverse fields to be measured, which would otherwise send the beam out of the spectrometer.

[H2] Muon Instrumentation

[H3] Muon spin spectrometers

All μSR spectrometers share several common features. First, there is either a muon detector or a pulse that defines the implantation of the muons into the sample. Second, an external magnetic field can be applied either parallel (longitudinal) or perpendicular (transverse) to the initial muon polarisation. Alternatively, compensation coils can be used to produce zero magnetic field at the sample. Third, positron detectors are arranged, ideally symmetrically, around the sample in order to reconstruct the time and spatial dependence of the muon spins inside the sample and hence the magnitude and fluctuation rate of the local magnetic field.

Muons are produced with their spins anti-parallel (surface muons) or parallel (decay muons) to their momentum. Applying a magnetic field transverse to muons with this spin orientation will lead to a deflection of the muon beam due to the Lorentz force **[G]** and limits the measurements to magnetic fields of less than ~25 mT otherwise the muon will miss the sample. A longitudinal magnetic field in this geometry does not deflect the muon beam since $v \times B = 0$ and so measurements can be made in magnetic fields of several Tesla (a schematic is shown in Figure 1e). Measurements in transverse magnetic fields up to ~10 T can be performed by applying a magnetic field along the initial muon momentum and rotating the muon spin perpendicular to its momentum prior to implantation (a schematic is shown in Figure 1f). The upper limit to the magnetic field is due to the positron Larmor radius **[G]** becoming so small that the positrons cannot reach the detectors. The addition of a magnetic field allows the state of the sample to be changed or to decouple the muon from a particular magnetic environment.

The muon polarisation is proportional to the asymmetry in the numbers of positrons detected in opposing pairs of detectors. The configuration of the positron detectors depends on whether one is performing transverse field (TF) or longitudinal field (LF) measurements and whether one can manipulate the orientation of the muon spin prior to implantation. Some μSR spectrometers are optimized for either high TF or LF experiments while others can be used for both types of measurement.

[H3] Low-energy muons

Muons originating from pion decay have a kinetic energy of about 4.2 MeV, and the penetration depth of muons with energies in the MeV range in solid matter is from sub-millimetres to centimetres (**Error! Reference source not found.** 1c). With these muons, the application of μSR is limited to studies of bulk materials. In order to extend μSR to nanometre-thin layers such as thin films, heterostructures, or near-surface regions, low-energy muons with energies in the keV range are required. Two techniques are currently pursued for this purpose[23]: two-photon ionisation of thermal muonium, and

a moderation technique based on cryogenic thin layers of van-der Waals bound solids. Both require surface-muon beams with high intensities (> 10^8 μ^+/s) to convert a small fraction (≤ 10^{-4}) of the incoming beam into "ultra-slow muons" with energies in the range of 0.2 – 20 eV. Post-acceleration by electrostatic fields then tune the beam energy in the range ≤ 1 keV – 30 keV.

BOX 2: Low-energy muon production.

Two-photon ionisation of thermal muonium in a vacuum is only possible at pulsed accelerators, where pulsed laser systems provide the required laser energy for efficient ionization of muonium, leaving an ultra-slow muon with an energy of about 0.2 eV. At J-PARC, the Ultra-slow muon (USM) beamline[24-26] is under development, where a pulsed surface muon beam at 25 Hz impinges on a 2000-K hot tungsten foil, from which a pulsed beam of thermal muonium atoms escapes into vacuum. The ionisation of muonium then takes place in two steps: one laser generates Lyman-α photons at 122 nm to excite the 1S-2P transition, and a second laser at 355 nm ionizes the excited muonium atoms.

At continuous and pulsed muon beam facilities, a moderation technique based on cryogenic thin layers of van-der Waals bound solids such rare gases and nitrogen significantly reduces the energy of the surface muons to 10 – 20 eV. In contrast to the laser ionisation method where 50% of the muon polarisation is lost in the initial muonium state, the muon polarisation is conserved in the moderation process. The most efficient moderators are solid neon and solid argon layers. The Low Energy Muons (LEM) facility at PSI routinely provides up to 2x10^4 μ^+/s. In 2006, LEM opened as a user facility with a user program for μSR applications on nanometre-thin layers (low-energy μSR, LE-μSR)[27,28]. /BOX2

[H3] External Stimulation

In the standard muon spectrometer, the sample is enclosed in a cryostat or furnace and the instrument has a fixed magnet, which can deliver a fixed range of fields. This enables the sample to be exposed to a range of temperatures (from ~20 mK to 2000 K). It is relatively easy to get muons into a sample by using thin cryostat (or furnace) windows, typically Mylar, aluminium or titanium. In addition to this, other stimuli can be applied, for example and not limited to: pressure, radio-frequency (RF), light and electric field. Due to the requirement to inject the muons through the wall of a pressure cell, and the size of the muon beam imposes a sample volume that limits, with the current technology, the applied pressure to ~2.8 GPa[29,30].

RF-μSR is complementary to the NMR technique. The RF firing timing can be controlled to synchronise with the injection of the muons or for a determined time later. Time dependence of fast changes in the electronic state is sensed within the μSR time range up to about 15 μs. The muon spin rotates during the application of RF in applied longitudinal fields. This technique can also be applied to measure the transverse muon-spin rotation in strong longitudinal fields[31], decoupling specific nuclei, pulse techniques [32] and measuring reaction rate constants[33]. A recent development has been the ability to stimulate a sample with photon irradiation. Early studies used flash lamps, however recent developments have used laser technologies[34,35,36]. Another technique is the application of electric fields which can manipulate the properties of the sample and investigate charge dynamics[37].

[H2] Elemental Analysis

In order to use muons for elemental analysis the negatively charged variety is required. Using negative muons, muonic X-rays are emitted which is dependent on the capturing atom. When a negative muon is implanted into the sample, it is readily captured by an atom in the material, thus forming a muonic atom **[G]**, with a capture probability approximately proportional to the atomic number *Z* and at an energy level **[G]** of ~ *n*=5. During this process the muon initially ejects Auger electrons **[G]** that are usually self-absorbed and not observed. After forming the muonic atom, the muon cascades down to the lowest energy level, *n* = 1. During each cascade, the muon emits an X-ray and given that the mass of the muon is ~200 times that of an electron, these X-ray emissions range from 10s of keV to 8000 keV. The energy resolution is determined by the detector technology, high-purity germanium, and varies as a function of energy from ~ 0.5 keV (at low energy) to 5 keV(at high energy). The K_α energies **[G]** are shown in **Error! Reference source not found.**2a and an example of a muon cascade in Figure 2b. These high energies allow for elements as light as lithium up to the highest Z to be relatively easily observed (note: helium and hydrogen can be observed but the low energy muonic X-rays makes self-absorption effects problematic). In addition, the elemental composition can be determined deep beneath the surface (Figure 2c and d, a more detailed discussion on these results will appear later). The main advantage over other techniques is it is non-destructive, sensitive to all elements (including light elements), can measure depth within the sample (i.e. not just the surface), can depth profile, from 10s nm to cms and does not make the samples active. This has resulted in the technique becoming highly attractive for areas e.g. cultural heritage, advanced manufacturing, energy materials and biosystems.

These instruments require decay channel muon beamlines and there are currently two muon facilities that are running user programs, ISIS and J-PARC, while the facilities at PSI, TRIUMF and MuSIC are developing this technique. The experimental setups are quite similar; they consist of a number of high-purity germanium detectors arranged around the sample, with a range of energy efficiencies and resolution. The notable difference between the ISIS and J-PARC setup is the vacuum chamber at the sample position at J-PARC. This enables a reduced background at the lowest incident muon momenta.

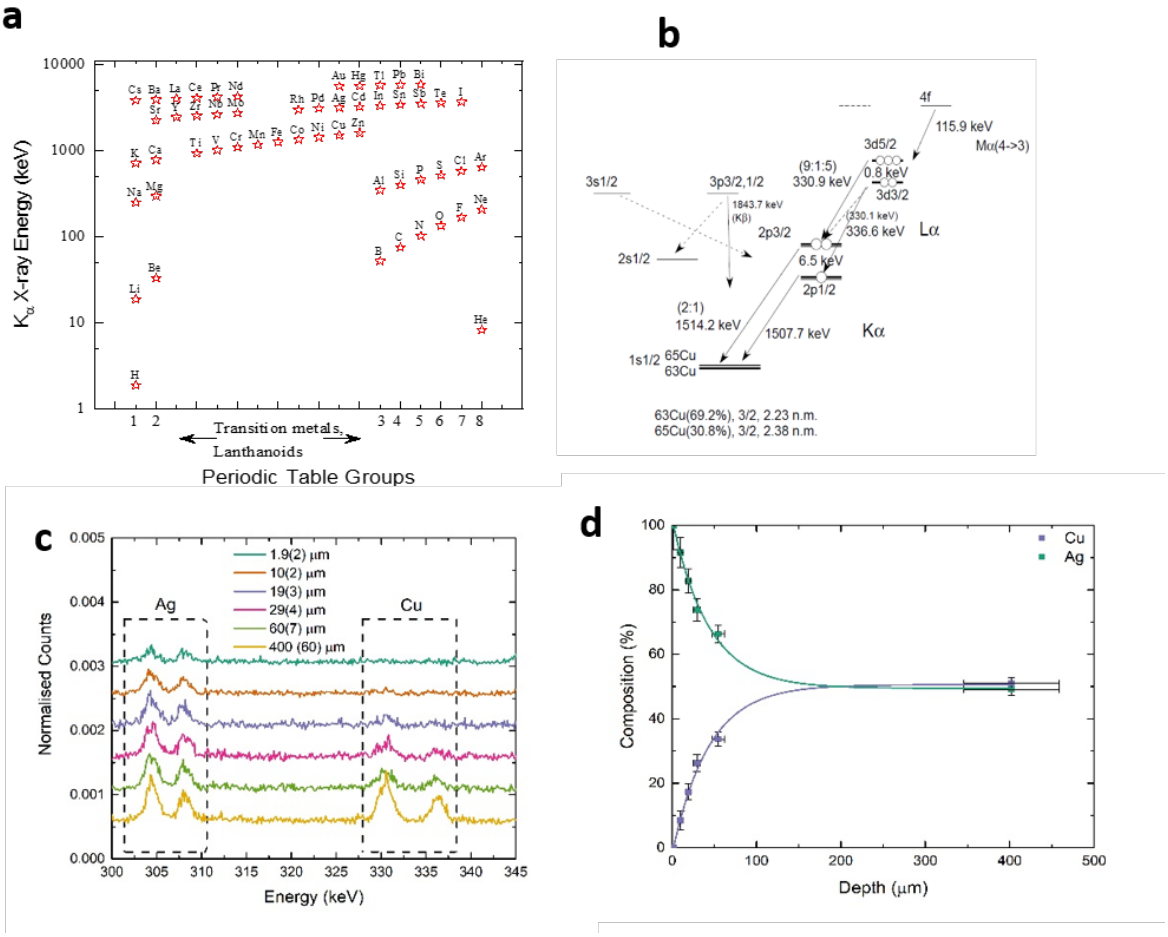

Figure 2: *(a) The muonic K_α emission energies for most stable elements in the periodic table. (b) The muon cascade after the initial capture showing the possible emission spectra from copper. The Kα, Lα and Mα transitions are the from electron shell n=2 to 1, n=3 to 2 and n-4 to 3 respectively. (c) The momentum dependence of the silver and copper muonic X-ray peaks in the energy range 300 – 345 keV. The momentum/depth is highest for the lower spectrum and lowest for the upper spectrum and clearly shows the lack of copper for the lowest momentum/depth and therefore nearest to the surface. (d) The depth dependence of the composition as determined from the data on the left. The data was taken from Hampshire et al Ref ([38]).*

The time (relative to the muon implantation) and energy of the X-ray emissions is determined. As the momentum of the negative muon beam is known then these measurements can be depth resolved[39,40], thus enabling a depth resolved compositional analysis. Recent developments have utilised highly-pixelated areas to directly image the sample under investigation; one approach is to place the detector as close as possible to the sample[41] and the other uses a pinhole camera approach[42].

[H2] Sample mounting

How a user mounts their sample can be the difference between a successful or unsuccessful experiment and should be given some thought before the experiment starts. There may be a difference between different facilities, but largely the same principles apply across the board.

Generally, one wants to use a sample holder which results in little relaxation of the muon polarisation. Therefore, one normally sticks to elements with small nuclear moments μ_N, examples of which are detailed in Table 1. However, some elements with large μ_N are used as they are cheap and easy to machine, but one must be mindful of this as if these elements are used, a correction will need to be added to the data for muons which stop in these materials rather than the sample. Many different sample holders exist across the different facilities. Common-place holders include simply gluing your sample onto a silver backing plate on the cooling stage of the cryostat, creating a silver foil packet, larger squares of aluminium, silver or titanium with shapes milled out for powders to sit within, or more specialist equipment. For sub-0.3 K measurements, small amounts of dilute GE varnish (a standard varnish with good thermal properties) can be poured on powder samples to help thermal conductivity.

Element\Isotope	**Abundance (%)**	**I**	**μ (μ_N)**
^{107}Ag	51.8	1/2	-0.114
^{109}Ag	48.2	1/2	-0.131
^{47}Ti	7.4	5/2	-0.788
^{48}Ti	73.7	0	0
^{49}Ti	5.41	7/2	-1.104
^{27}Al	100	5/2	3.641
^{63}Cu	69.2	3/2	2.223
^{65}Cu	30.8	3/2	2.382
^{1}H (Plastics)	~100	1/2	2.793
^{56}Fe (Stainless Steel)	91.8	0	0
^{52}Cr	83.8	0	0
^{53}Cr	9.6	3/2	-0.475

Table 3: Common elements used to make sample holders with the nuclear moment of their main isotopes shown.

Other more exotic methods for containing or mounting examples are available, for example: cells for air-sensitive samples and for liquids, although the same considerations pointed out above apply. One can also have large sample cells for gaseous samples, where you require a large amount of gas to stop the sample. Experiments studying muonium **[G]** or muoniated radicals in liquids and gases require O_2 be removed before encapsulation as O_2 can react rapidly with these paramagnetic species. O_2 can be removed by repeated cycles of freeze-pump-thawing or by bubbling with argon for an extended period. Lastly, it is worth mentioning pressure cells that have been developed at different facilities[29,30]. These tend to require large amounts of sample and the pressure medium can either be through an oil

or gas and one has to bear in mind that the cell itself may have a muon relaxation rate which is temperature dependent.

[H1] Results

This section discusses different ways to reduce and analyse data for the range of experimental setups, from time differential (in both geometries: longitudinal and transverse), avoided-level crossing muon spin spectroscopy and elemental analysis, along with some standard software packages. More detailed description can be found in the standard textbooks [6,11] and [7].

[H2] Muon implantation

The first step of a μSR experiment is the implantation of muons into the material of interest. The muon enters the sample with a relatively high energy (typically between 4 and 40 MeV). The muon rapidly thermalizes in the sample. The first stages reduce the energy to 2-30keV by ionisation of the atoms and scattering with electrons (Δt~10^{-9}s), the next stage is the formation of muonium through successive electron capture and loss (Δt~10^{-13}s) and during this process energy of the muon is further reduced to ~ 50 eV. The final stage is the muonium-atom collision and the dissociation of thermalized muonium yielding a thermalized muon. Once in a thermalized state, the muon is a 'free' muon (a diamagnetic state), i.e. it localises at an interstitial site in the crystal structure, or picks up an electron to form muonium (a paramagnetic state, Mu). In this case, the muon can be considered as a light isotope of hydrogen and is chemically very similar (Bohr radius, a_{Mu}= 1.004a_H, ionisation potential, I_{Mu}=0.996I_H, but with a reduced mass, m_{Mu}=1/9m_H). The final possible state is a muoniated radical (a paramagnetic state) where the muon is chemically bound in a molecule containing an unpaired electron. The state that muon forms depends, critically, on the sample under investigation and by forming these states different information can be obtained. For example, for most metallic and/or magnetic systems a 'free' muon is found, for some semiconductors and insulators muonium can be formed, and for systems that have unsaturated bonds a muoniated radical may form. The state of the muon can change on the timescale of the μSR experiment. In all cases, the muon will interact with its local environment and the muon will decay into a positron or electron (μ^+ or μ^-) preferentially along or opposite the final spin direction. By monitoring the polarisation, information about the material of interest can be obtained.

[H2] Time differential muon spectroscopy

Since there is usually, at any given time, only one muon in a sample at a continuous facility and up to a few thousand muons in a volume of ~0.5 cm^3 at a pulsed facility, we do not need to consider muon - muon spin interactions in the sample. The spin precession of the muon can be measured by measuring the positron (or electron) emitted after μ-e decay. These detectors, simply, are constructed with a fast scintillating material, light guide and photo-multiplier tube or Si-photo-multiplier. From this the light is converted into an electrical signal, which is time-stamped, often to picosecond timing. When applying the μSR method to various materials, whether with continuous or pulsed muons, the time-differential method is the most common method.

A positive muon implanted in a sample is resting at an intermediate position in the crystal and decays into a positron and two neutrinos with a half-life of 2.2 μs[43]. The muon spin is in principle 100% polarised, and the positron is emitted preferentially in the spin direction, $W(\theta) = 1 + A\cos\theta$, where θ

is the angle between the muon spin and the direction of the positron emission, and *A* is energy dependent and on average is approximately 0.3.

Time-differential μSR can be classified into three types depending on the presence or absence of an external magnetic field and its direction.

1) ZF (Zero Field) measurement

   No external field (less than 5 μT) is applied. By taking advantage of the 100% polarisation of muons, this measurement is a unique method to find antiferromagnetism, which is difficult to observe by macroscopic methods. In addition and importantly, the volume fraction of any magnetic transition can also be measured.

2) LF (Longitudinal Field) measurement

   An external field is applied parallel to the initial muon polarisation. By measuring at different external magnetic field values, it is possible to obtain rough values of the internal magnetic field distribution or dynamics or the hyperfine structure **[G]** of muonium formed in the material. The muon spin relaxation rate provides information about dynamics processes in the sample.

3) TF (Transverse Field) measurement

   An external field is applied perpendicular to the initial muon polarisation. The muon spin precesses around the total field at the muon site.

A diagram of a μSR spectrometer is shown in **Error! Reference source not found.**1e and 1f. The blue arrow indicates the muon that arrive from the left side and rests in the sample, with spin antiparallel to the momentum (surface muons). The detectors are placed before (forward) and after (backward) the sample.

For zero field and longitudinal field experiments, the time evolution of the positron, *N(t)*, count can be expressed by the following equation,

$$N(t) = N_0 \exp\left(-\frac{t}{\tau_\mu}\right)\left(1 + a_0 P_z(t)\right), \quad \text{(Eq 7)}$$

where $P_z(t)$ is the polarisation function, which is 100 % polarised (for μ^+) at t = 0, and changes with time depending on the interaction with the sample. The a_0 term is the empirical maximum from the spectrometer (see **Error! Reference source not found.**3a for an example of the positron counts as a function of time). The polarisation $P_z(t)$ is equivalent to the longitudinal relaxation **[G]** function, $G_z(t)$. In order to determine $P_z(t)$ or $G_z(t)$ the counts in the forward and backward detectors are summed (N_F and N_B respectively) and evaluated by,

$$a_0 P(t) = a_0 G_z(t) = \frac{N_F(t) - \alpha N_B(t)}{N_F(t) + \alpha N_B(t)} \quad \text{(Eq 8)}$$

where α is a calibration constant (see **Error! Reference source not found.**3b for an example of a typical asymmetry spectrum). By analysing this expression, information about the interaction with the sample

at the muon site can be obtained. Common functional forms for $G_z(t)$ are the Kubo-Toyabe function[44], a damped cosine, an exponential decay and combinations thereof[6,8,11,13].

For transverse field experiments, the polarisation function becomes (sometimes multiple terms have to be summed),

$$P_x(t) = G_x(t)\cos(\gamma B_{TF} t) \qquad \text{(Eq 9)}$$

where γ is the gyromagnetic ratio of the muon and B_{TF} is the transverse magnetic field. The functional form of $G_x(t)$ and changes to B_{TF} yield information on the sample under investigation. This is commonly used in Knight-shift measurements and superconductivity. Clearly, if oscillations are observed in either longitudinal or transverse experiments further analysis can be useful, for example: Fourier transforms or Maximum entropy techniques[45].

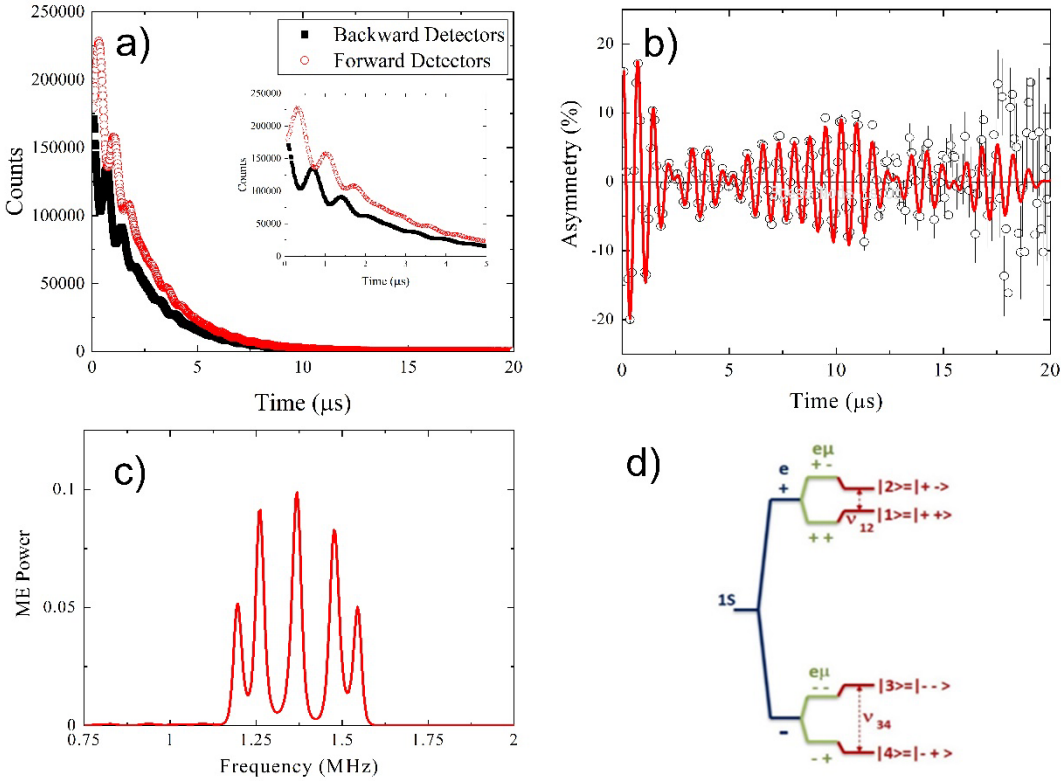

Figure 3(a) The position counts as a function of time, summed into forward and backward detectors. (b) μSR time spectrum for an undoped CdS single crystal at 4.1 K, under an external magnetic field of B=0.01 T. The field direction is perpendicularly to the muon spin and parallel to the hexagonal <0001> axis of the sample. (c) Fourier Maximum Entropy transforms of the time spectrum in (b)[45]. The Larmor precession frequency of the Mu^+ charge state is at the center of two additional pair of lines, associated with a weak muon-electron bound state, a neutral Mu^0 of a shallow defect center. The muonium lines are due to transitions between hyperfine energy levels of Mu^0 spin states in the high-field limit regime, consistent with a hyperfine tensor with axial symmetry along the Cd-S bond direction[46]. (d) Sketch of the splitting of the Mu^0 spin states in the high field limit, illustrating the contributions of electron Zeeman energy (blue), muon Zeeman energy (green) and hyperfine coupling between the muon and the electron (red). The + and – signs indicate spin up and down, respectively. Each pair of muonium lines observed in (b) and (c) correspond to state transitions

$|1\rangle \leftrightarrow |2\rangle$ *and* $|3\rangle \leftrightarrow |4\rangle$*, for two different orientations of the Cd-S bond relative to the applied field.*

[H2] Avoided level crossing muon spectroscopy

Avoided level crossing muon spectroscopy (ALC-μSR) is used to characterize muoniated radicals **[G]** by measuring the muon hyperfine coupling constant **[G]** (in the solid state) and nuclear hyperfine coupling constants **[G]**. Measuring the muon and nuclear hyperfine coupling constants allows one to map out the distribution of the unpaired electron, which can be used to identify the structure and conformation of radicals[47]. The more hyperfine coupling constants one can measure, the more you know about the structure of the radical.

For these experiments, the muon asymmetry is determined by integrating the counts in the forward and backward detectors. At specific values of the applied field, which depend on the values of the hyperfine coupling constants, nearly degenerate pairs of spin states are mixed through the hyperfine interaction. The muon polarisation oscillates between the two mixing states and results in a resonant-like change in the asymmetry as the magnetic field is swept. Two types of resonance are commonly observed and are characterized by the selection rule $|\Delta M| = 0$ and 1, where M is the sum of the quantum numbers for the z-components of the muon and nuclear spins. The shorthand notation commonly used are Δ_0 and Δ_1 resonances, respectively.

Δ_0 resonances are observed for muoniated radicals in solids, liquids, or gases. The resonance field for a Δ_0 resonance is given by

$$B_{res}^{\Delta_0} = \frac{1}{2}\left[\frac{A_\mu - A_x}{\gamma_\mu - \gamma_x} - \frac{A_\mu + A_x}{\gamma_e}\right] \qquad \text{(Eq 10)}$$

where A_x is the nuclear hyperfine coupling constant and γ_x is the nuclear gyromagnetic ratio[48]. The nucleus X could be anything with non-zero spin, such as H, D, ^{13}C, ^{14}N, ^{19}F, ^{31}P etc. In Figure 4a there is the ALC-μSR spectrum of the Mu adduct of ^{13}C-labelled C_{60} in decalin solution. There are a number of resonances due to hyperfine coupling between the unpaired electron and the ^{13}C nuclei. The position of the resonances is used with Eq 10 to calculate the ^{13}C hyperfine coupling constants. This provides information about how the unpaired electron is distributed around the C_{60} sphere.

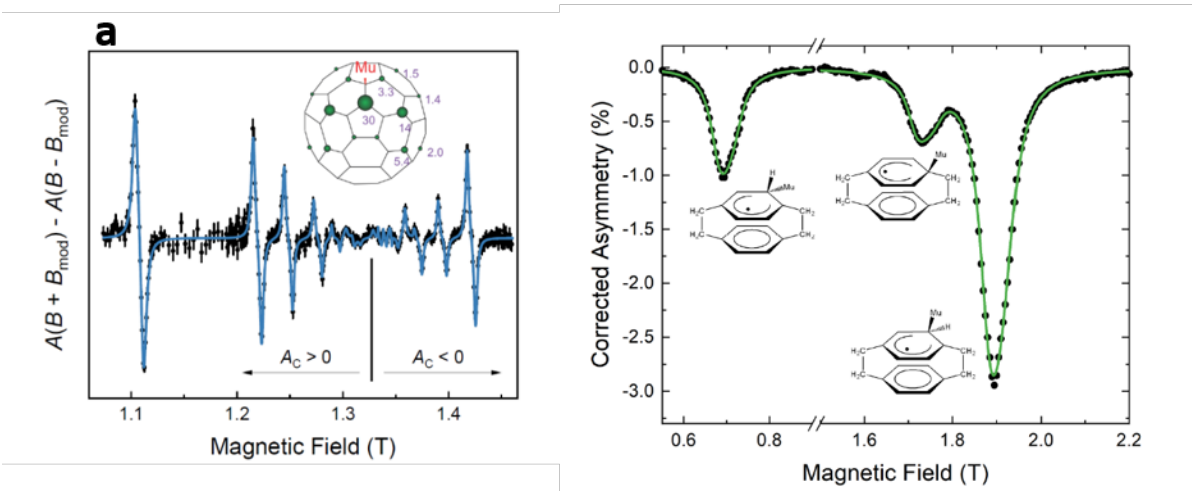

Figure 4 (a) ALC–μSR spectrum of the Mu adduct of ^{13}C-labelled C_{60} in decalin solution at 293 K. There are multiple Δ_0 resonances due to the hyperfine coupling with ^{13}C nuclei around the sphere and the hyperfine coupling constants were used to map out the distribution of the unpaired electron (shown in %). The spectrum was obtained with magnetic field modulation, which results in the resonances having a differential lineshape. Data from Reference Percival et al[49]. (b) ALC-μSR spectrum of [2.2]paracyclophane at 300 K showing the Δ_1 resonances of the three types of muoniated radical (as shown by the chemical image insets). Data from Reference McKenzie et al[50]. The positions of the resonances give the A_μ of each radical, the widths and line shapes provide information about the dipolar muon hyperfine coupling and the amplitudes give the relative yield of each radical.

Δ_1 resonances are only observed when muoniated radicals are undergoing anisotropic motion on a critical time scale given by the inverse of the hyperfine anisotropy (typically ~50 ns for organic radicals). The Δ_1 resonance field only depends on A_μ and is given by

$$B_{res}^{\Delta_1} = \frac{1}{2}\left[\frac{A_\mu}{\gamma_\mu} - \frac{A_\mu}{\gamma_e}\right]. \qquad \text{(Eq 11)}$$

The lineshape of the Δ_1 resonance can be sensitive to the reorientational motion of the muoniated radical[51]. The position of the Δ_1 resonance is used to determine A_μ using Eq 11 and the lineshape can provide information about the anisotropic dynamics. In Figure 4b there are three Δ_1 resonances due to three types of muoniated radical, which are formed by Mu addition to [2.2]paracyclophane.

[H2] Elemental Analysis

The analysis of the composition using negative muons is relatively simple. The intensity of the muonic X-ray peak is directly related to the elemental composition in the sample. However, there are other contributions that can affect the intensity of the peaks, in particular, the probability of muon capture, the cascade transition rates **[G]** and detector efficiency[52]. The probability of muon capture is, as a first estimate, proportional to the number of electrons (Fermi-Teller approximation) and in the majority of cases this is satisfactory. However, in oxygen-based systems this approximation can be inconsistent. For these systems additional correction terms have been added to take into account the number of loosely bound electrons and the number of valence electrons. Another important factor is the muon cascade probability **[G]**. A schematic of the cascade for copper is shown in **Error! Reference source not found.**2b. This again will affect the intensities of the muonic X-rays. In general, best practice is to spend time in each experiment measuring certified standards that are close to that which is expected. This enables comparisons of electronic transitions of the different energy levels within the atom, such as: Kα, Lα, Mα and other muonic X-rays (for example see **Error! Reference source not found.**2c). This also takes into account the detector efficiencies and self-absorption if measured carefully.

During the final nuclear capture process the muons can undergo a reaction with the proton and release a neutron(s) and photon. The release of this neutron can lead to an unstable nucleus which

subsequently leads to the release of gamma rays. The energy of this gamma ray is of the same magnitude as the muonic X-rays, although the lifetime is generally longer allowing for relatively easy determination. This can lead to the potential of isotope analysis[53].

[H2] Software for analysis

There is a wide range of software available for the analysis of muon spin spectroscopy data, each package is in various stages of development, functionality, sustainability and maintainability. Each muon facility has at least one preferred analysis package. The major analysis packages are MuSRFit[54],Wimda[55] and Mantid[56]. These packages automatically include a number of corrections that need to be applied to the muon spectra, for example, background, time zero (time of muon implantation) and deadtimes corrections. Training can be found by online learning (e.g. Baker *et al*[57]) and assistance from your local instrument scientist.

[H1] Applications

This section highlights some of the key areas that muon spin spectroscopy has been particularly successful. These examples are Magnetism, Quantum Systems, Superconductivity, Energy Materials, Physical Chemistry, Dynamics in Soft Matter, Semiconductors, Surface science, Cultural Heritage and the effects of muons on electronics. Within each of these sections, key scientific results are discussed and examples are highlighted. In particular, the muon being a local probe often gives unique information not obtainable by any other technique and the muons' sensitivity to very weak internal magnetic fields increases its complementarity to other techniques, e.g. neutron scattering, NMR and ESR.

[H2] Magnetism

One of the most important applications of muons is in studies of magnetism. In contrast to many other techniques, you don't need to apply a magnetic field to obtain a signal: μSR can be performed in zero magnetic field. Then, any precession signal in the polarisation of the implanted muon arises from the internal magnetic field measured at the muon site; thus, the temperature dependence of this precession frequency yields the temperature dependence of the order parameter. This makes the muon a very efficient indicator of magnetic order (extracting both its strength and the magnetic volume fraction in the sample, from the frequency and amplitude of the precession signal). For this reason, many of the magnetic phase diagrams in new material families are often first established by μSR, the iron-based superconductors being prime examples [58-60]. Because the muon probes the entirety of the sample, it is not affected by tiny impurity phases (in contrast to magnetic susceptibility); this feature permitted the discovery of superexchange via the hydride ion using μSR in a system in which nanoscopic elemental cobalt was present as a very minor impurity[61].

The muon is also an effective probe of the dynamics of the magnetic moments within a sample. Before materials enter a magnetic ground-state, one will often observe a critical slowing down of the magnetic fluctuations. Generally this will be observed as a divergence of the muon spin relaxation rate on cooling through the transition and can be an effective way of probing the dynamic nature of transitions[62-67], and providing information on systems where the magnetism is dominated by excitations[68]. Additionally, this approach can also be used to pick apart short and long range order,

where the coupling of the muon to its local environment provides complementary, and sometimes, unique information to other techniques[69-72].

Being able to establish bulk magnetic order allowed μSR to demonstrate this in the very first organic ferromagnet[73,74] which is based upon free radicals; here muonium attacks the radical and the diamagnetic signal is thought to originate between a singlet state comprised of the muonium electron and the radical electron [74]. However, some of the most interesting applications of this technique have been in low-dimensional magnetic systems. No long-range order is possible in one dimension, but magnetic chains (with intrachain exchange J) occur embedded in crystals and the weak interchain interactions allow long-range order to occur, albeit at much lower temperature than J/k_B and with reduced moments[75]. In such systems the thermodynamic signatures of long range order are strongly suppressed [76], but μSR can easily identify them from the onset of a precession signal (see **Error! Reference source not found.**5a-b) and thus new transitions in molecule-based magnets have been discovered[77], as well as the best examples of one and two dimensional Heisenberg antiferromagnets identified and characterized [78,79]. These results have been extended to molecular spin ladders[80] and organic molecules showing magnetism and superconductivity[81].

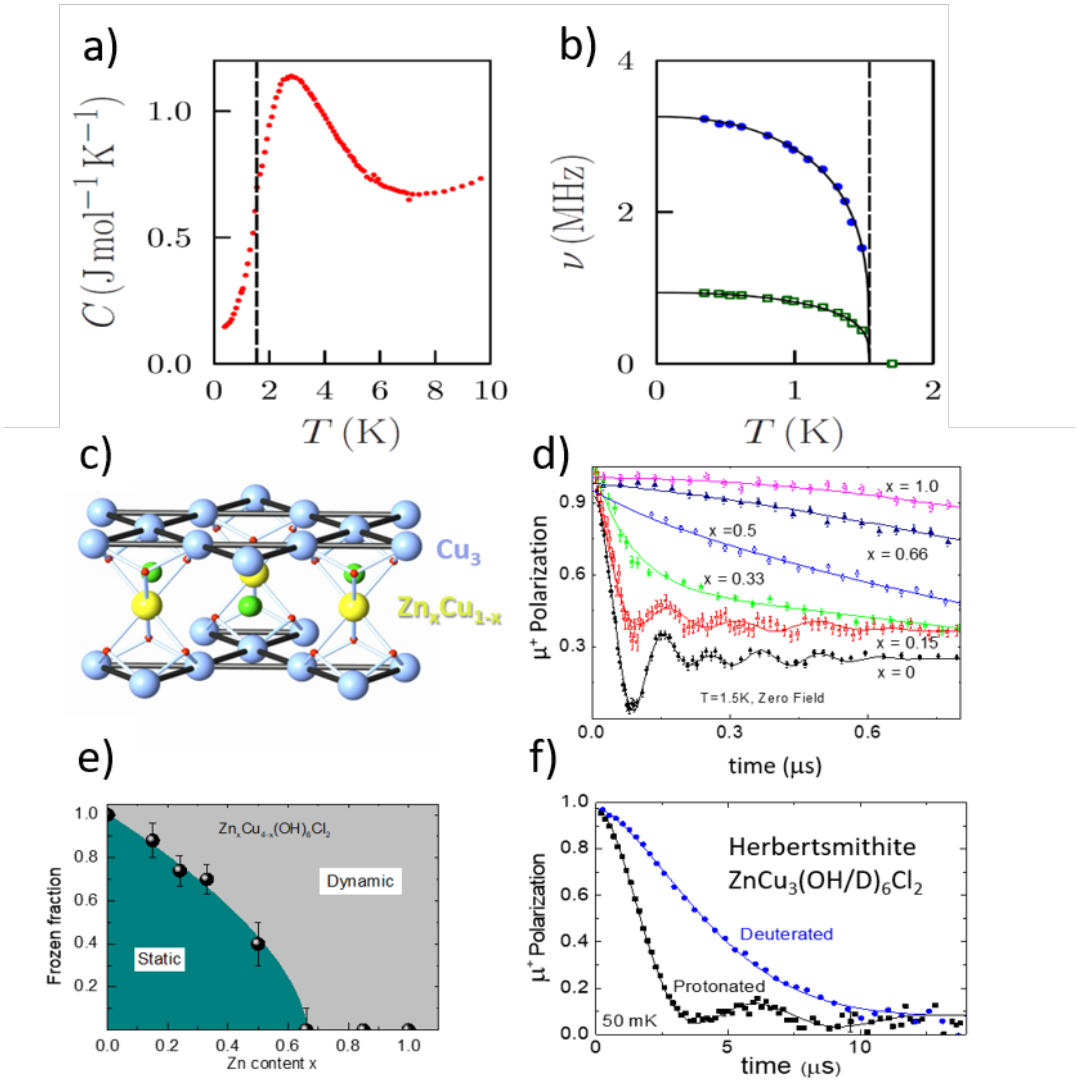

Figure 5: (a) Heat capacity and (b) μSR precession frequencies measured in [Cu(HF2)(pyz)2]BF4 (where pyz=pyrazine). The broad peak in the heat capacity is due to the building up of correlations in the two-dimensional planes. Three-dimensional long-range order only sets in once the inter-plane interactions become important, but the transition to long-range order (indicated by the vertical dashed line in both figures) is not clearly visible from the heat capacity data. In contrast, a clear precession signal consisting of two frequencies is found in muon experiments and these data allow the order parameter to be tracked. [Adapted from J. L. Manson et al.[82]] c) crystal structure of the paratacamite compounds. The spin liquid candidate herbertsmithite is obtained for x=1, when the Cu based kagome planes are separated by diamagnetic Zn. d) The muon depolarisation spectra shows the static internal fields vanish progressively as x is increased. e) Magnetic phase diagram of the paratacamite drawn from the μSR data shown in d). Adapted from ref Mendels et al.[83]. f) In herbertsmithite (x=1) the relaxation is mostly due to quasi-static nuclear magnetism.

Much recent progress has been made in characterizing well-known magnetic compounds such as MnSi in which exquisite agreement between experiment and theory is obtained[84]. μSR has also been used to study various quantum phase transitions[64,85,86], systems with coupling between magnetism and the lattice[87] and frustrated magnetic ground states[88,89]. Most studies have been in the bulk, but low-energy muons offer the possibility of studying magnetism in thin films and surfaces. A future possibility is to use this to perform proximal magnetometry of spin fluctuations by implanting muons close to a magnetic surface [90].

Interesting effects can also occur when the magnetism is not electronic, but nuclear. A muon implanted in a fluoride results in a state in which the muon resides between two fluorine ions: F-μ-F [91]. An oscillatory time dependence of the muon polarisation can result from the entanglement of muon and nearest-neighbour spin-1/2 fluorine nuclear spins that arises due to the magnetic dipolar interactions [91,92]. More distant nuclear spins in the system can result in a decohering effect and can also be modelled quantitatively, allowing a very detailed description of the decoherence processes coupling this F-μ-F "system" with its "environment", and providing a model realisation of the quantum decoherence problem[93].

[H2] Quantum Systems

In quantum magnets the rotational symmetry of the spins is preserved in the ground state. This differs from classical magnets with long range ordered spins and spin glasses, which all feature on-site static moments at low temperature. This also differs from paramagnets because strong correlations exist between the spins, leading to non-trivial ground states and exotic excitations. Implanted muons allow scientists both to select, with unique accuracy, magnetic materials with a ground state dominated by quantum fluctuations, and to probe the nature of their original excitations.

To favour such quantum states, the quantum fluctuations have to be strongly enhanced which is best achieved in low spin S=1/2 materials such as the widely studied cuprates and S=1/2 molecular magnets or, less commonly, vanadium[94] or titanium-based oxides[95]. Alternatively, effective quantum spins may be realized in heavier transition metal oxides with large spin-orbit coupling, like iridates, or in the low energy physics of some rare-earth based magnets.

The dimensionality of the spin system is one other important parameter for quantum magnetism. In spin chains or spin ladders compounds, the low dimensionality efficiently suppresses the development of long range order in favour of quantum ground states at least in the quasi-1D regime of the material, when the temperature is larger than the inter-chain or inter-ladder residual interaction[77]. µSR is uniquely suited to single out the relevant –most often low- energy scales which require low-sub Kelvin- and non-perturbative zero-field experiments.

In higher dimensions, avoiding long range order is more challenging. It requires a high level of frustration of the magnetic interaction which can arise from competing interactions, the geometry of the lattice as in well studied kagome materials featuring a corner-sharing triangular magnetic lattice[83], or strongly anisotropic, bond dependent, interactions as in Kitaev materials[96]. The various quantum ground states expected in such conditions are generically dubbed "quantum spin liquids". One common signature of these quantum spin liquids is the absence of static magnetism, even at T=0 K. The unique sensitivity of µSR to tiny static internal fields makes it an ideal probe to test this simple requirement[83] and is now commonly applied to newly discovered spin liquid candidate materials at the early stage of their investigation[97]. In particular, µSR has proved invaluable to reveal subtle magnetic ordering with weak frozen moments, disordered spin glass-like state, and/or inhomogeneous ground states that are often realized in low dimensional frustrated material which fail to retain a spin liquid state[98] or which are driven beyond a quantum critical point by external pressure[96] or applied fields[88]. **Error! Reference source not found.**c-f shows how static long range order is suppressed progressively upon Zn doping of the antiferromagnet $Cu_4(OH)_6Cl_2$. For intermediate doping, both a paramagnetic phase and a frozen, strongly disordered, magnetic phase coexist. In the herbertsmithite spin liquid end member, only the static nuclear magnetism depolarises the implanted muons. The electronic spins are fast fluctuating or entangled in a nonmagnetic singlet ground state.

In ideal cases, beyond asserting the absence of frozen magnetism, the detailed study of the dynamical relaxation, how it evolves with temperature and applied longitudinal field, can shed light on the nature of the excitations[99,100]. These excitations are often exotic in quantum disordered materials[80] –either confined or unconfined, from neutral fermion forming a metal-like Fermi sea to Dirac or Majorana fermions, with a gap or gapless spectrum - and often characteristic of the otherwise elusive nature of the spin liquid state.

[H2] Superconductivity

The discovery of superconducting cuprate and Fe-pnictides compounds with high transition temperature (T_c) have fuelled a flurry of research into superconductivity. There have been huge theoretical and experimental efforts to understand the mechanism of unconventional superconductivity and to search for higher temperature superconductors, due to the potential widespread applications of superconductor materials. Muon spin rotation/relaxation has proved an effective probe of superconductivity in many different classes of materials.

Transverse-field (TF) μSR has been widely utilized to probe the internal magnetic field distribution in the vortex state of type-II superconductors[101,102]. In a TF-μSR experiment, spin-polarised positive muons are implanted into a sample in an external field perpendicular to the initial muon spin polarisation. Each muon precesses around the local field at its site, and the functional form of the

muon spin polarisation depends on the field distribution of the flux-line lattice of the vortex state, which is determined by the magnetic penetration depth λ, the vortex core radius *r*, and the structure of the flux-line lattice. The muon spin relaxation rate is related to the root mean square (rms) width of the internal magnetic field distribution in the flux-line lattice. In turn, the rms width is inversely proportional to the square of the magnetic penetration depth λ, which is related to the density n_s of superconducting carries and m^* by the London equation[103]

$$1/\lambda^2 = \mu_0 n_s e^2/m^* \qquad \text{(Eq 12)}$$

Therefore, the temperature dependence of normalized superfluid density can be measured by TF-μSR, and the functional form of $n_s(T)$ depends on the gap symmetry. Evidence of *d*-wave superconductivity for cuprate[104] and multiple gap symmetries for the order parameter without nodes for Fe-pnictides[105] have been given. The famous Uemura plot, in which T_c is plotted as a function of effective Fermi temperature evaluated from $1/\lambda^2(0)$, as determined by μSR, established universal behaviour for different categories of superconductors, covering dynamic superconductivity observed recently[106,107]. In high TF-μSR experiments, the precession frequency in a paramagnet is shifted from its value in vacuum. The fractional frequency shift, Knight shift, provides a microscopic characterisation of the static magnetization. In a superconducting state, Knight shift includes the contribution from spin susceptibility and therefore the study of it also provides crucial information about the pairing symmetry of cooper pairs[101].

Whether time-reversal symmetry (TRS) is broken or not is one of the important properties of superconductivity[108]. In a superconducting state with broken TRS, the Cooper pairs have nonzero magnetic moment. These moments align locally, and result in extremely small internal magnetic fields. To detect such spontaneous small magnetic fields, zero-field μSR is one of the most powerful methods, since it is especially sensitive to small changes in internal fields and can often measure fields of 10 μT, equivalent to a precession frequency of 1.5kHz[101,109]. In the absence of magnetic order, the muon spin polarisation is relaxed only by static randomly orientated nuclear dipole moments, and the relaxation rate is temperature independent. If a weak spontaneous internal field appears below T_c, one observes an increase in the relaxation of muon spin polarisation, where the increase in relaxation corresponds to an order parameter. TRS-broken superconducting states are quite rare, μSR has successfully detected this phenomenon in a number of unconventional superconductors, such as the layered perovskite superconductor Sr_2RuO_4 [110], noncentrosymmetric $LaNiC_2$ [111], the filled skutterudite compounds $PrOs_4Sb_{12}$ and $PrPt_4Ge_{12}$ [112,113]. There has been a recent topical review of the muon results in time-reversal symmetry breaking superconductors[114].

There is growing evidence for the coexistence of superconductivity with either ferromagnetic or antiferromagnetic ordering. So far there is no unified theory for the coexistence of superconductivity and magnetism, and the interplay of magnetism and superconductivity has been a central problem in condensed matter physics. Because of μSR's high sensitivity to internal magnetic fields on a microscopic scale, and its ability to determine the volume fraction of the magnetic and superconducting phases, and the temperature or doping dependence of order parameters, it has been successfully applied to study the interplay of magnetism and superconductivity in a variety of

unconventional superconductors. For example, a μSR investigation of a iron pnictide $SmFeAsO_{1-x}F_x$ with x = 0 - 0.30 shows that static magnetism persists into the superconducting regime[59]. On the other hand, a μSR study showed that magnetic order region competes with the superconductivity in $La_{2-x}Sr_xCu_{1-y}Zn_yO_4$ system [111,115]. In addition to static magnetism, the μSR technique is also capable of detecting dynamic magnetism and has revealed slowly fluctuating magnetic fields in the pseudogap region of the high-temperature superconducting cuprates[116].

[H2] Energy Materials

In this section, we demonstrate the ways in which μSR can be applied in the research about energy materials, such as electrode materials for lithium-ion batteries and hydrogen storage materials. In battery electrode materials, Li^+ ions diffuse between regular lithium sites and vacant sites (**Error! Reference source not found.**6a) and this diffusion is a key factor for the determination of the charge and discharge rates of a battery.

The time scale of Li^+ ion diffusion in battery materials is within the time window for μSR technique[117,118]. Although Li-NMR is a suitable probe to detect ion diffusion, signals from magnetic ions such as Co and Fe, which is mostly included in battery materials, hinders observation of Li^+ ion diffusion. In the μSR technique, responses from Li^+ ion diffusion and magnetic ions appear with completely different frequencies to be distinguished. As mentioned below, Li^+ ion diffusion determines the time required for charging of a battery. Therefore, μSR is a unique probe to contribute fast battery through observation of Li^+ ion diffusion in battery materials. Here is a rough estimation of the time window. Considering that Li^+ ions move from the centre of a cathode particle of r=5 μm diameter to the surface within t=ten minutes, a self-diffusion coefficient of Li (D_{Li} < 1/(6t)*(r^2)) is estimated to be greater than 10^{-11} cm^2/s . In fact, D_{Li} of various cathode materials, i.e., $LiMO_2$ (*M*: transition metal), were found to range between 10^{-12} and 10^{-9} cm^2/s at a nominal room temperature with μ^+SR[119-133]. Specifically, the implanted muons can locate the interstitial sites near O^{2-} ions and detect the internal magnetic field formed by the nuclear magnetic moments of lithium and *M*. The ZF-μ^+SR spectrum for $LiMO_2$ usually exhibits a well-known Kubo-Toyabe (KT) type relaxation behaviour (**Error! Reference source not found.**6b), and such a spectrum can be easily decoupled with a small longitudinal field (LF), typically below 1 mT, comparable to the field distribution width at the muon sites. When lithium starts to diffuse, the relaxation rate is suppressed owing to "motional narrowing"(**Error! Reference source not found.**c). A similar diffusive behaviour is also exhibited by sodium-ion battery materials [134,135]. A recent study using μSR with negative muons (μ^-SR) on $LiMnPO_4$ has clarified that such a behaviour is not caused by μ^+ diffusion but by Li^+ diffusion [136], because μ^-s are captured by the nucleus and information about nuclear magnetic fields is typically provided from fixed viewpoints and shows the complementary use of both positive and negative muons is useful in studies on ion diffusion.

Graphite and various carbon materials are used as anode materials in Li-ion batteries. Based on first principles calculations, it is predicted that the implanted μ^+s can form a stable C-H like bond with carbon. As a result of this, μ^+SR will provide D_{Li} in Li-intercalated graphite, such as C_6Li and $C_{12}Li$, in anode sheets [137,138]. We envisage the observation of lithium diffusion in an operating battery using the unique penetration depth of the muon beam in the near future. Actually, a kind of "in situ" measurements is being realized[139], and great progress in a battery research with μSR is expected.

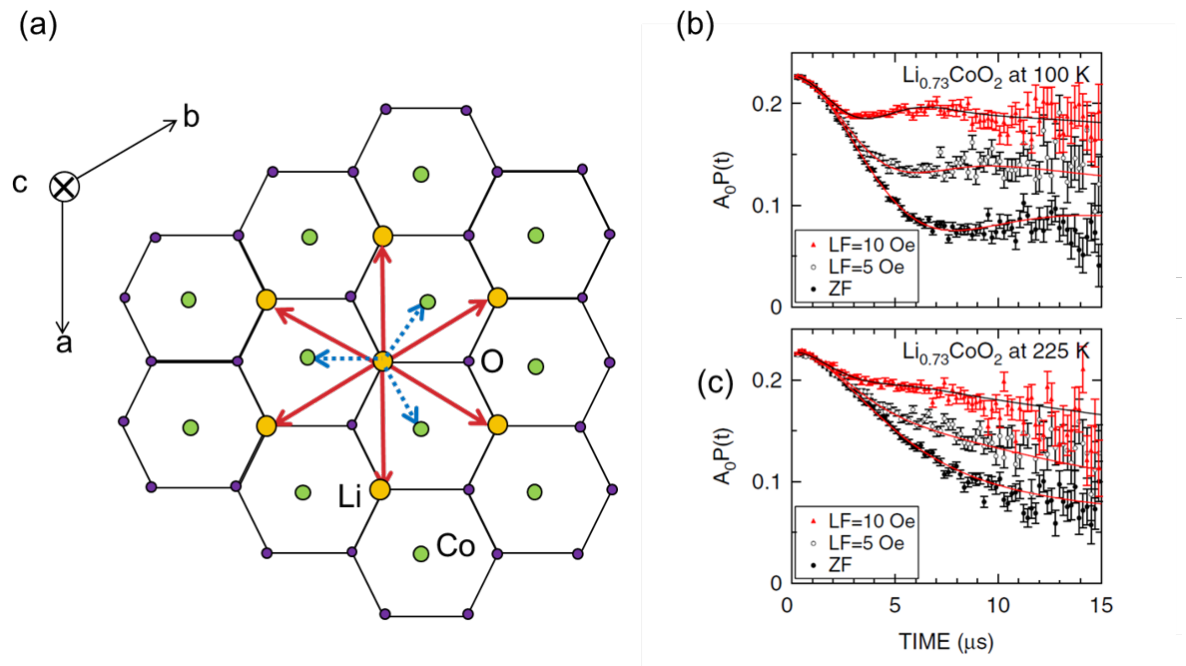

Figure 6 (a) Schematic of the path for Li diffusion in Li_xCoO_2. The ZF-μ^+SR spectrum exhibiting a Kubo-Toyabe type relaxation for $Li_{0.73}CoO_2$ (b) at 100 K (static) and (c) at 225 K (dynamic). These are reproduced from Ref. [119] published by the American Physical Society.

The technique of μSR is also a good tool to detect hydrogen diffusion in hydrogen storage materials during desorption reaction with controlling temperature, since lower hydrogen desorption temperature (T_d) is required for hydrogen storage materials. A pioneering μ^+SR study has been reported on $NaAlH_4$, in which a three spin-1/2 system H-μ-H is formed [140]. Then, the formation of H-μ-H (and H-μ) were found in numerous hydrogen storage materials including MgH_2 (Supplementary **Error! Reference source not found.**1a and b)[141] through observation of a characteristic oscillation in the ZF-μ^+SR spectrum (**Error! Reference source not found.**1c). A recent *in-situ* μ^+SR work on MgH_2 [141] demonstrated that such a H-μ-H system disappears above room temperature and that the ZF-μ^+SR spectrum instead exhibits a KT type relaxation behaviour (Supplementary **Error! Reference source not found.**d). Additionally, with further increase in temperature, hydrogen starts to diffuse below T_d (**Error! Reference source not found.**e) [141]. To decrease T_d, it is important to enhance hydrogen diffusion in MgH_2 in order to release the desorbed H_2 from the system [141]. Research on μ^-SR with MgH_2 has also supported the presence of H diffusion in MgH_2 [142].

[H2] Physical Chemistry

The main uses of μSR in physical chemistry are to study the reactions of muonium (Mu = [μ^+e^-]) and to characterize free radicals[47]. Muonium is studied because it is similar and yet different from hydrogen. The similar chemical behaviour of Mu and H means that Mu is studied in conditions where one can't study H, such as in pressure cells. High-momentum muons are highly penetrating and the decay positron, which provide the information about the evolution of the muon's spin polarisation, are energetic enough to escape the pressure vessel. Mu can also be generated cleanly whereas H atom formation by radiolysis produces multiple reactive species, such as ·OH, e_{aq}^-, HO_2·, and H_2O_2 in water, which requires the addition of scavengers and complicates analysis.

The main difference between Mu and H is the light mass of Mu (1/9 that of H), which can lead to large isotope effects that provide information about the mechanism of the reaction being studied. For example, the addition of Mu to benzene in the gas phase[143] is over an order of magnitude *faster* than that of H or D addition[144] at room temperature (**Error! Reference source not found.**a), due to tunnelling **[G]** playing a dominant role. This should be compared with the Mu + $CH_3OH_{(aq)}$ abstraction reaction **[G]** [145], which is approximately two orders of magnitude *slower* than the H + $CH_3OH_{(aq)}$ reaction (**Error! Reference source not found.**7b)[146,147]. Abstraction reactions typically have barriers that are too wide for tunnelling, and the inverse kinetic isotope effect (i.e. the reaction being slower for the lighter isotope) is primarily due to the activation energy for the lighter isotope being larger due to higher zero-point vibrational energies **[G]** in the transition state[148]. The Mu + $CH_3OH_{(aq)}$ reaction was studied to much higher temperatures than was possible for H + $CH_3OH_{(aq)}$ and this made it possible to observe deviations from Arrhenius behaviour close to the critical point of water. The temperature dependence of H + $CH_3OH_{(aq)}$ reaction rate can be predicted from the results of the μSR measurements.

μSR can be used to characterize the structure and dynamics of radicals in a way that is similar to electron paramagnetic resonance (EPR)[47]. Transient radicals have important roles in chemistry, such as intermediates in reactions, but are difficult to study with most conventional spectroscopic techniques due to their short lifetimes. Radicals can be identified by measuring the muon and nuclear hyperfine coupling constants, which map out the distribution of the unpaired electron, and then comparing these values with ones obtained from ab initio calculations. Information about dynamics as well as the conformation can be obtained by measuring the temperature dependence of the hyperfine coupling constants.

μSR has several advantages over EPR when studying transient free radicals. (1) Muoniated radicals are produced in situ and they do not require harsh chemicals (for example Fenton's reagent) or radiolysis with electrons or γ-rays. (2) Muons arrive with almost 100 % spin polarisation, so very low quantities of muoniated species can be detected (10^7, cf. 10^{12} spins for ESR, 10^{18} for NMR). (3) μSR does not require an external electromagnetic field to stimulate spin-level transitions. (4) Very short-lived radicals can be detected. (5) EPR measurements of transient free radicals can be difficult at higher temperatures as bimolecular termination reactions lead to a loss of signal. By contrast, at any given instant there are only a few muoniated radicals in a sample, which means that bimolecular termination reactions can be ignored. This makes it possible to study radicals under conditions where they are highly mobile, such as at high temperatures. (6) Finally, muoniated radicals are usually the primary product of the Mu addition reaction. This is advantageous as EPR spectra are frequently complicated by secondary and later products.

μSR has difficulty dealing with systems with multiple unsaturated bonds. The relative yield of different muoniated radicals depends on the number and reactivity of the different functional groups in the parent compound(s). This does provide a means of probing the reactivity of a parent compound, but the more radicals that are formed, the more difficult it is to characterize them as the polarisation will be distributed among them, which results in lower signal amplitudes.

Consider the reaction of Mu with a phosphaalkene (**1**), which is a molecule with a P=C bond[149]. Mu could add to either the phosphorous atom or the carbon atom and generate the radicals shown in **Error! Reference source not found.**7c. Two types of muoniated radical were observed in the TF-μSR spectrum (**Error! Reference source not found.**7d) and they have very different yields. There were two resonances at lower magnetic fields (Supplementary **Error! Reference source not found.**2a) due

to hyperfine coupling with phosphorous and one resonance at a higher magnetic field (Supplementary **Error! Reference source not found.**2b) due to hyperfine coupling with the protons of the two methyl groups. The magnitude of the muon, phosphorous and proton hyperfine coupling constants were used to assign the structures, and this was aided by a comparison with a structurally related radical. **1b** was determined to be the major product and **1a** was the minor product.

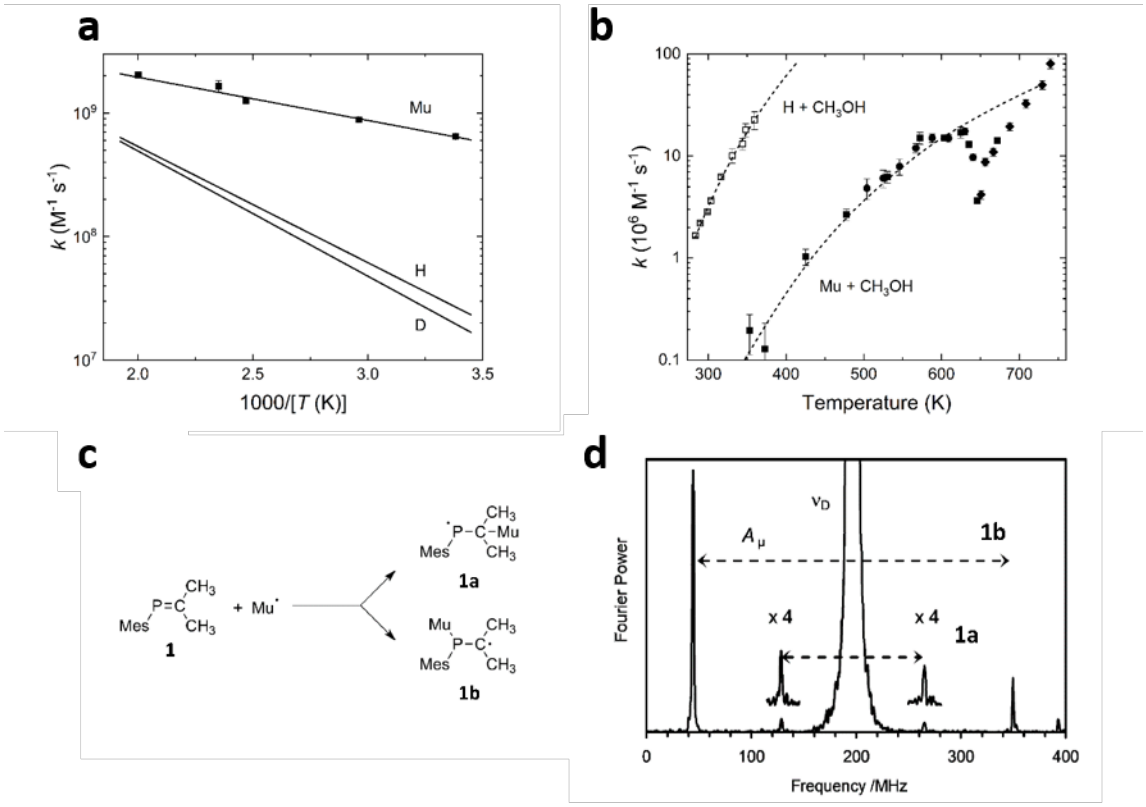
a
Mu
H
D
1000/[T (K)]
b
H + CH3OH
Mu + CH3OH
Temperature (K)
c
1
1a
1b
d
νD
Aμ
1b
x 4
x 4
1a
Fourier Power
Frequency /MHz

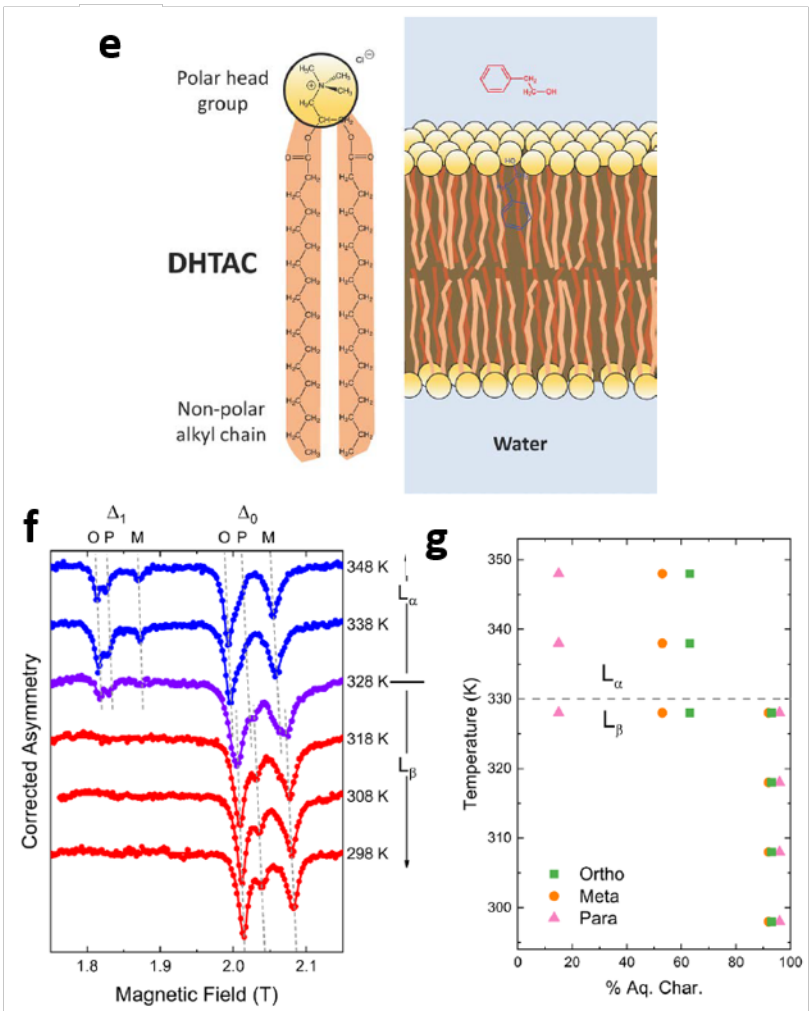
e
Polar head group
DHTAC
Non-polar alkyl chain
Water
f
Δ1
Δ0
O P M
O P M
348 K
338 K
328 K
318 K
308 K
298 K
Lα
Lβ
Corrected Asymmetry
Magnetic Field (T)
g
Lα
Lβ
Ortho
Meta
Para
Temperature (K)
% Aq. Char.

Figure 7: (a) Arrhenius plots for the addition reactions of Mu, H and D to benzene in the gas phase. The data for Mu is from E. Roduner et al.[143] and the H and D data is from J. M. Nicovich and A. R. Ravishankara,[144]. b) Rate constants for the reaction of Mu with methanol in water at ~230 bar and H with methanol at ambient pressure. The Mu data is from K. Ghandi et al.[146] and P. W. Percival et al. [147]. The H data is from S. P. Mezyk and D. M. Bartels[145] . (c) Structures of phosphaalkene (1) and the possible muoniated radicals (1a and 1b). (d) TF-μSR spectrum of a solution of phosphaalkene 1 in thf. Figure reproduced from reference [149]. (e) Structure of DHTAC and a schematic of the bilayer with the locations of PEA in the low-temperature Lβ phase and high-temperature Lα phase shown. (f) ALC-μSR spectra of PEA in DHTAC bilayers. The labels O, M and P refer to the muoniated radicals formed by Mu addition to the ortho, meta and para carbons of the phenyl ring of PEA. Data from Reference [150].
(g) Local polarities determined from the Δ_0 resonance fields. Data from Reference [150].
(e) Low-field portion of the ALC-μSR spectrum of a solution of phosphaalkene 1 in thf.

[H2] Dynamics in soft matter

Studying the dynamics of molecular units is vital to understanding the properties of soft matter, such as liquid crystals and biomembranes. Mu will add to unsaturated bonds in soft matter to produce muoniated spin labels in specific sites that are sensitive to the local environment and dynamics. The muoniated radicals, which are present in extremely low concentrations, are small perturbations to the system while fluorescent probes and nitroxide spin labels, have been found to significantly alter the properties of membranes[151]. The site-directed muon spin labelling plus the sensitivity of μSR to motion on different timescales compared with NMR and X-ray and neutron scattering means μSR can provide unique and complementary information from other techniques.

We will consider an example of molecules interacting with bilayers, which could be fragrances interacting with soap, or drug molecules interacting with biomembranes. DHTAC (**Error! Reference source not found.**e) is a molecule that has hydrophobic and hydrophilic functional groups and can self-assemble in aqueous solution to form different structures such as "lamellar" liquid crystalline phases where the surfactant molecules form arrays of regularly separated bilayer "sheets" separated by solvent[152]. The addition of cosurfactants can result in subtle changes in the microstructure of the bilayer, which in turn can have dramatic effects on macroscopic behaviour (for example see Safinya[153]). The cosurfactant can also have additional roles, such as being a fragrance or a pharmaceutical, and are typically present only in very low concentrations (~ mM), which makes them difficult to study using traditional spectroscopic methods[154] .

ALC-μSR can be used to determine where the cosurfactant is located. We will consider the cosurfactant 2-phenylethanol (PEA), which gives an odour of roses, in DHTAC bilayers[150] (Figure 7e-g). Muoniated radicals are formed by Mu addition to the ortho, meta and para carbons of the phenyl ring of PEA. Muoniated radicals aren't formed by Mu addition to DHTAC as Mu addition to C=O bonds are ~100 times slower than to phenyl rings. The hyperfine coupling constants of the Mu adducts of PEA, and hence the Δ_0 resonance positions, are sensitive to the polarity of the local environment of PEA. Shifts of the Δ_0 resonances in a range of solvents were used to determine the "aqueous character" of the environment ranging from water (100% aqueous) to $C_{18}H_{38}$ (0% aqueous).

DHTAC forms bilayers that undergo a structural change at 329 K; below this temperature, the system is in the L_β phase where the motion of the alkyl chains is limited, and above this temperature the system is in the L_α phase where the alkyl chains have considerably more mobility. In the L_β phase there are three Δ_0 methylene proton resonances but no Δ_1 resonances, which indicates the motion of the radical, and the cosurfactant, is isotropic. The % aqueous character of the three isomers is close to 100% (**Error! Reference source not found.**f). Both facts indicate that PEA cannot penetrate the bilayer in the L_β phase due to the tight packing of the alkyl chains and resides in an aqueous environment. Δ_1 resonances are observed in the L_α phase, which indicates that the motion of the radicals is anisotropic, and the Δ_0 resonances have shifted to a lower magnetic field, which indicates a lower % aqueous character. The results indicate that PEA resides within the DHTAC bilayer in the L_α phase. This is a consequence of the higher mobility of the alkyl chains in the bilayer. At 328 K, which is near the L_β – L_α transition, PEA resides in both the bilayer and the aqueous region.

The pharmacological effect of a drug depends on its mechanism of action, or the way it interacts with the different components of the body. Similar measurements to those described here could be performed to spin label drug molecules and then study the partitioning of drug molecules between aqueous environments such as cell fluids and lipid-like environments of a model cell membrane or the interaction between a drug molecule and the model cell membrane[154]. One could also label components of a model cell membrane, such as cholesterol, and study dynamics within the membrane and investigate the formation of lipid rafts.

[H2] Semiconductors or hydrogen in materials

Muons are used in semiconductor research as a model for the behaviour of the isolated hydrogen impurity, in cases where direct access is hard or impossible, as well as a local probe for charge carriers and defects.

Hydrogen is an unavoidable contaminant in most semiconductors, since it is easily incorporated in all steps of the material handling, from growth to processing. In addition to the formation of complexes, hydrogen can be present in semiconductors as an isolated, monoatomic impurity, most commonly playing a compensating role. Although isolated hydrogen has an important electrical activity, when present in very low concentrations it is often not accessible by conventional techniques, making the μSR technique a unique and privileged tool. When the positive muon is incorporated in the semiconductor, it may bind to an electron and form muonium, which behaves as a light isotope of hydrogen with very similar electronic properties. Muon implantation inside a semiconductor material creates muonium impurities in the high-dilution limit **[G]** , with three possible charge states, Mu^+, Mu^0, Mu^-, mimicking the charged states of isolated hydrogen (H^+, H^0, H^-). The correspondence between the hydrogen and muon impurity centres is well supported by the few cases where the experimental observation of both systems was conducted, namely in Si, ZnO and TiO_2 [155-160]. Most of the existing information on the role of isolated hydrogen in both elemental and compound semiconductors is actually provided by the μSR technique, namely concerning Mu configuration, position of electronic levels, interaction with carriers as well as passivation of impurities and defects[161]. Prior to μSR results, hydrogen was known to occupy interstitial positions in the host material, either as a neutral or a negatively charged centre (H^-/H^0), introducing an acceptor level in the band gap. Among the numerous

contributions of μSR to the physics of hydrogen in semiconductors, a mention is due to the discovery and characterization of two other possible isolated hydrogen configurations, where it incorporates the bonding structure of the lattice. One is a bond-centre configuration, first observed and extensively characterized in silicon by μSR, together with the corresponding deep donor level[155,161]. The second one was the finding of a shallow donor state in some materials, where the muon (or the proton) stabilizes in an antibonding position, close to an anion[46,156]. μSR results in ZnO constituted the first experimental confirmation of a theoretical suggestion that hydrogen would be a cause of n-type doping in this important material[156] (see **Error! Reference source not found.**3).

More recently, the use of muons as a local probe to charge carriers and defects in semiconductors is being explored. One route is the direct interaction with charge carriers in photo-excited samples. Recent examples include the measuring of excess carrier lifetimes[162] and the observation of the hole carrier density profile at a film surface[36]. A different route relies on the sensitivity of the relative fractions of the different muon charge states to the defect content of the material and the possibility to obtain depth-resolved information on defective layers in films, using slow muons[163,164].

[H2] Surface science

The application of low energy muons (LE-μSR) to thin films and near-surface studies is still a growing field. One of the most straight-forward applications is the measurement of magnetic field profiles at the surface of superconductors to directly determine the penetration depth and coherence length[165-168], the shape of domains in type-I superconductors[169], or to measure proximity effects between superconducting and non-superconducting thin layers (metals, ferromagnetic layers, topological materials)[170-175]. These studies reveal the strength and sensitivity of LE-μSR in determining magnetic field profiles with a nanometre resolution at interfaces, which allowed new insights in anomalous proximity effects – such as the newly discovered electromagnetic proximity effect[172-174] – and induced odd-frequency superconductivity[171,175].

The effect of dimensionality and strain on the magnetic and superconducting properties of thin film heterostructures is another wide field of applications of LE-μSR. Two pioneering works showed the drastic effect of dimensionality on the magnetic order. The first work demonstrated, by combining optical ellipsometry and LE-μSR, that paramagnetic and metallic $LaNiO_3$ could be controlled to become insulating and antiferromagnetically ordered, if the layer thickness is reduced to two unit cells, independent on the strain of the film[176]. In this quasi-2D system, the tendency towards charge and spin order is supposed to be due to enhanced nesting of the $LaNiO_3$ Fermi surface, similar to bulk $RNiO_3$, where R is a small radius anion rare earth. The second work showed, that for La_2CuO_4 layers, the long-range magnetic order breaks down for less than five layers of CuO_2, where a magnetic state evolves with enhanced quantum fluctuations and reduced spin stiffness[177]. Surprisingly, the state exists in close proximity to a superconducting layer without transmitting supercurrents. In other complex cuprate metal-oxide correlated electronic systems, an interplay between quasi-2D superconductivity and magnetism was observed in superlattices of δ-doped La_2CuO_4 [178]. Single layers of SrO_2, periodically inserted in a lattice of LaO_2 layers, provide the charge doping to turn the interface to the LaO_2 layers superconducting. A non-trivial coupling of the superconducting state (T_c ~25 K) to

the antiferromagnetic order (T_N = 325 K) occurs: below T_c there is a strong increase of the magnetic volume fraction. This is attributed to a charge redistribution of free carriers at close proximity between the different layers when the superconducting gap opens. The effect of strain and defects on the magnetic transition temperatures was investigated in a series of experiments on cuprates[179] and manganites[180-182]. Defects typically cause a reduction of magnetic transition temperatures, whereas strain can lead to both increase and decrease, depending on the type of strain.

Films of dilute ferromagnetic semiconductors (DFS) are important for spintronics applications. The magnetic homogeneity of these films is of paramount importance. With LE-μSR, it is straightforward to measure the magnetic volume fractions of these systems, which allows determining the appropriate growth and annealing conditions to generate homogeneous systems[183-186]. If the film thickness is less than 100 nm, the muons can be implanted in the substrate to measure the magnetic stray fields from the ferromagnetic layers. The size of the stray fields and the length scale of its disappearance yields information about the interface roughness and the multi-domain character of the film[186,187].

Due to its unique strength of localising the region of magnetic moments inside heterostructures, LE-μSR provided significant information for spin diffusion in organic spin valves[187], the emergence of ferromagnetic order at metal/C_{60} interfaces[188], spin-storage in metal-oxide/C60 interfaces[189], and depth dependence of spin dynamics in molecular magnetic systems [190,191]. In semiconductor physics, LE-μSR extends the classical μSR application of characterizing hydrogen impurities to new directions: investigation of defect regions at interfaces in solar cell materials[163] and in 4H- SiC[164] to provide microscopic information to improve those interfaces for device applications, and to study band bending[192] and charge carrier profiles and their manipulation at semiconductor surfaces[36].

These examples represent some of the highlights of LE-μSR applications. There are much more possibilities and we refer readers to the LEM facility web site[193] for a complete list.

[H2] Cultural Heritage

Recent developments at muon facilities have shown a resurgence in using μSR to analyse materials with a cultural heritage interest. It is of particular interest to use this technique because it is sensitive to all elements (H and He are challenging), can probe 'deep' within a sample, be depth dependent and most importantly completely non-destructive. A nice recent example of the potential of this technique was the investigation of debasement of coinage from various historical perspectives[38]. A particular period of interest is that of the Roman Empire, where 'silver' coinage were actually a silver-copper alloy and coins were subjected to heat treatment and oxidation to enrich the surface, allowing for the silver composition to vary from 100% to as low as 20%[194,195] . It is argued that establishing the composition of these coins yields new and valuable information about the fiscal health of ancient nations. The results from Hampshire *et al*. show the extent of the surface enrichment as shown in **Error! Reference source not found.**2c-d[38]. However, it would appear that the gold coinage was left untouched, even in times of great turmoil[196].

However, other gold coinage has been surface enriched. An example of this is a coin from the Tempo-Koban (19th Century CE) in which the core composition is approximately 57 wt% gold and 43 wt% silver[197]. A recent study of votive lamps fragments in the form of small ships have shown a range of compositions of Cu-Sn-Pb[198]. Although, these examples are metallic samples, there is no reason why organic materials cannot be investigated. An early example of this is the modern and archaeological fired clays[199] and biomaterials[200,201]. This clearly shows the versatility and general application of the technique to all materials, whether that be cultural heritage or not. A more detailed review can be found in reference[202].

[H2] Effects of muons on electronics

The effects of neutron and alpha radiation is well known in electronics and are probably the most dominant radiation-induced failure (neutron mostly on earth, proton and heavy ions in space). The primary source of cosmic radiation is high energy protons (~87% creating neutrons and muons), the remainder is alpha particles (~11%) and high-energy electrons (~1%). On the earth's surface, muons (resulting from the interaction of high energy proton) contribute to about 75 % of the dose rate. These muons are, generally, very high energies and in the range of 1-20GeV. However, as electronic technologies reduce in size and power the risk of negative effects from singly-charged particles, in particular muons, can increase. In older technologies, charged particles such as muons travelling through the device did not disturb the atomic environment significantly enough for a soft error **[G]** to occur[203]. However, as the technologies reduced in size more of these soft errors were observed. In order to understand the effects of muons on electronics, and where the electronics are most sensitive, the implantation depth was controlled. A peak in the error rate was increased when the muons were implanted directly into the active electronic layer[204,205]. These 'soft errors' were further enhanced when the bias voltage was decreased, something that is desirable by the end user as it enables battery power devices to last longer. Furthermore, it has recently been found that the error rate was enhanced with negative muons[206]. Experiments at muon facilities provide valuable insights into these errors in a short and controlled timescale, which support the development of new and reliable electronics.

[H1] Reproducibility and data deposition

The raw data is usually stored at the facility, with a range of access policies. At the start of each experimental cycle the instruments are calibrated. This would include ensuring the focus of the beam is optimised for each instrument, and checking that the detectors, the data acquisition systems, the electronics are functioning properly. In addition, this would also include the determination of the time the muon enters the sample (known as t_0), and at pulsed sources the deadtime of each detector. This calibration data should be readily available and may be stored in the data files.

When reporting the results from a muon experiment you should cite the facility (this may be a data doi), the instrument or instrument(s) used and the setup of the instrument/beamline. To be able to ensure reproducibility, the author(s) should also include the sample environment used and how the sample was mounted. When reporting the sample environment it is beneficial to be specific about which piece of equipment is used. This enables the exact setup to be able to be reproduced in the future. Each facility has a standard format with readers that are freely available, unfortunately each has its own preferred format. The data is made freely available to all on the facilities web sites (this

might be after an embargo period e.g. three years to ensure a PhD thesis can be completed). The data files themselves are relatively small, at most only a few MB.

[H1] Limitations and optimizations

In this section, we discuss aspects that you should consider to ensure the experiment is successful. There is also a section on how to obtain beamtime at a muon facility.

[H2]Time window

There are two primary considerations for any experiments. Firstly, as for every technique, are the muons measuring in a frequency range that is of interest? Muons have a very broad time-window when measuring relaxation time (see **Error! Reference source not found.**8a) ranging from 10^{-4} to 10^{-11} s. However, each type of muon facility has also has its optimised region to work in. Generally, for fast relaxations and/or high precession frequencies a continuous muon source is optimal. However, for slower relaxations and the need to measure to many muon lifetimes and/or low frequency pulsed stimuli then a pulsed muon source maybe optimal. Of course, there is a wide overlapping range of each facility and even beamlines.

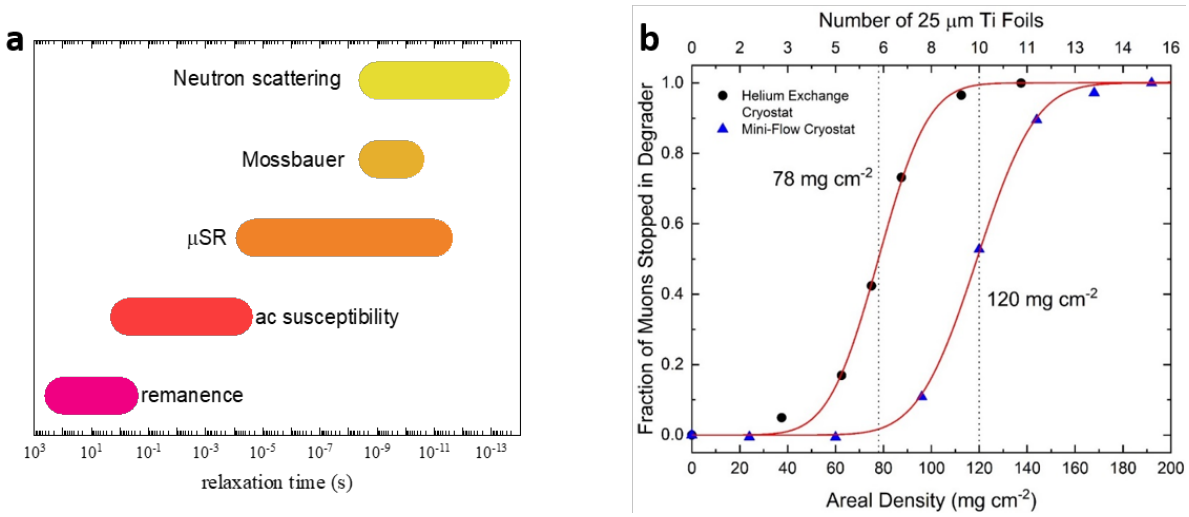

Figure 8: (a) The time-window of various techniques. This highlights the versatility of muons and also the limitations. (b) Degrader curves for two different sample environments taken on the ARGUS spectrometer within the RIKEN-RAL facility at the ISIS Neutron and Muon Source using 25 μm Ti foil. The dotted lines show the median value for each degrader curves, which shows the areal density at which the majority of muons are stopped within the degrader, or in reality, the sample. In an ideal experimental situation, one must aim to have enough areal density to stop all the muons within the sample, which would correspond to the point where the fraction of muons stopped in the degrader material is equal to one.

[H2] Sample size and mass

The mass and the size of the sample are important considerations for sample mounting. For example, a small sample with a big sample holder can be problematic and it may be more beneficial to create a silver foil packet to contain the sample. This is where a competition between beam spot size, experimental statistics and the areal density of your sample comes into play. In many facilities one can vary the beam spot size, but this is normally at the cost of count rate. To optimise this, one must consider the range for the instrument in a specific sample environment via a degrader curve. The degrader curves in **Error! Reference source not found.**8b were made by using a haematite plate, where titanium foils were added to probe the stopping profile of the muon beam in two different sample environments, often this will change temperature, pressure, or both. Even external stimuli samples environments can be developed. From this one can deduce the median value required to stop the majority of the muons and the areal density needed to stop all the muons within the sample. This is dependent on the beamline, cryostat and the number of beam windows. If one does not have enough sample to stop all the muons, degrader in the form of titanium, silver or mylar foils can be used. If one is interested in transverse field measurements, a way to minimise the background term is to actually mount a sample on a hematite plate. The muons that stop in the hematite are dephased extremely rapidly and so one does not see them within the muon spectra.

If one has particularly small samples, for a facility or beamline (usually a few mm's x mm's), then there are two main methods. The first is to use fly-past, where the sample is mounted on a holder similar size as the sample and the excess muons are able to fly-past the sample into a long tube further down from the instrument, where their decay has no/limited impact on the measurement. The second is to use a veto-method, such as that at PSI and TRIUMF, where muons that stop outside the sample are detected but can be vetoed and not counted within the spectra.

[H2]Access to facilities

The available beamtime for muon experiment around the world is fairly limited given there are currently only five operational muon facilities. Each facility has a range of access mechanisms: rapid access for urgent studies (not limited to: very topical material, short life of the sample, data needed for a thesis and/or publication, etc), industrial access, and the most common route of a general access call. The general access calls are usually twice per year, and at a similar time each year (the calls may vary due to operational timescale of the proton accelerator). It is strongly recommended that you visit the facilities' websites (for links to the facilities website see Ref [207]). For all of these panels, the proposals are peer reviewed and the highest rated proposals are taken forward for experiments. These proposals are usually short in duration, i.e. for a few days of beamtime and are from individual groups or collaboration. These groups can be, and often are, from around the world. New users to the facilities are always welcome and are often considered favourably within each panel.

[H1] Outlook

The future for muon spin spectroscopy is looking very encouraging. There are various strong developments, including new data analysis techniques, new instruments and new facilities. The

current facilities are planning to remain in operation for the foreseeable future, and there are new facilities being planned, including at the CSNS, China[208]; RAON, South Korea[209]; and the SNS, USA[210].

[H2] Possible Future Sources and Instruments

The EMuS facility at the CSNS will be a pulsed muon facility. However, unlike current pulsed facilities, the target for muon production will not be an intermediate target prior to a neutron target, but will be a dedicated target taking the full proton beam into a long carbon target. In order to obtain the highest intensity of muons a high-field (1 T for surface muons and 5 T for decay muons/pions) a capture solenoid is planned[211]. This will deliver either surface or decay muons to three experimental areas. Prior to this target, a 'thin' target is envisaged for surface muon extraction. The time structure of the EMuS source is a repetition rate 2.5 Hz, a pulse length of 50 ns and nominal power of 5 kW. It is intended that the initial spectrometer will have 128 detectors (64 forward and 64 backwards), however, the next generation is being planned with 2560 detectors[212]. This muon source will give a very high instantaneous data rate, which may be ideal for pulsed and/or in-situ experiments.

The RAON facility is an new accelerator complex[213]. The main science goal of this new complex is the understanding of elements. This will result in a heavy ion accelerator. In addition to this, a muon spin spectroscopy facility is being actively considered. This would be a continuous muon source with a surface muon beamline, similar to those at PSI and TRIUMF.

The SNS muon facility is developing a laser extraction at the end of the linear accelerator[214]. This will neutralise the H^- ions giving H^0. These will travel to the SNS linac dump and result in a 30 ns pulse at 50 kHz. This should enable a very high flux, which is optimised for the muon lifetime. It also allows for a muon source that does not require an intermediate target that can 'spoil' the proton beam and allows the target to be fully optimised for muon production.

Instruments at existing muon facilities undergo constant small improvements to enable better and broader range of science. However, there are regularly larger developments such as major upgrades and/or new instruments. There are three major projects currently underway: FLAME (at PSI), Super-MuSR (at ISIS) and M9A/M9H (at TRIUMF). All of these instruments will significantly advance the muon technique and enable new and unique science.

1) The FLAME instrument at PSI which will have a broad temperature (20mK to 310 K) and field range (0 to 3 T), small samples (with virtually no background), an increased time-resolution, and multi-stage sample holder for faster sample changes[215].

2) The Super-MuSR instrument at ISIS will have the addition of a muon pulse slicer to improve timing resolution at the pulse muon facility, greater number of detectors to improve positron count rates, and a spin rotator for improved transverse field experiments[216].

3) M9A is a surface muon beam line that will include a dedicated 3T spectrometer equipped with APD detectors that will be optimized for rapid sample characterization with user-friendly operation. M9H will be a decay muon beam line with both longitudinal AND transverse polarisation. Its end station will have a configurable spectrometer that encompasses a dilution refrigerator and more conventional sample environments. Both LF and TF-μSR measurements over wide ranges of magnetic fields (0 – 4 T), temperatures (40 mK – 500K) and pressures (i.e. up to 3 GPa) will be available within the set of sample environments being planned.

4) Future ISIS instrument plans include the improvement of an elemental analysis instrument. MuX, which should improve the counting rate by 10-1000, momentum and energy range dependent. This should be achieved by increased segmentation and will allow the full use of the incident muon flux.

5) PSI started a feasibility study to investigate the possibility of using state-of-the-art Si-Pixel detectors to determine the vertex of the muon decay with ≤ 1 mm precision. Such a "vertex reconstruction" will allow experiments to be performed at one order of magnitude higher beam rates, overcoming the pileup problem at continuous muon sources. It will enable new research directions for μSR by much faster, higher statistics and more efficient measurements (measuring several samples simultaneously), introducing lateral spatial resolution, and being able to apply external stimuli (pressure, light intensities, electric fields) at unprecedented levels (due to the fact that samples sizes can be reduced to < 1 mm).

These new instruments and facilities are extremely important developments for the future of muon science and are the key enablers for future work and ideas, e.g. reducing the size of samples required, needing more extreme environments, or more complex set-ups, e.g. in-situ experiments.

[H2] New techniques

[H3] DFT+mu

A problem that has dogged the μSR technique for many years is that although one can measure precisely the magnetic field (from both nuclear and electronic magnetism) at the muon site, the position of that site is not known a priori. There are various approaches that are being used to tackle this.

Perhaps one of the most simple, the MUESR package, is based on using "dipole-field and dipole-tensor sums using real space algorithms" to solve the problem of the muon site[217]. The program is able to quickly and quantitatively solve the magnetic field at given muon sites. MUESR was able to reproduce the observed fields at four different stopping sites within the compound, $CuSe_2O_5$, with good accuracy[218].

A more complex method is to use density functional theory, as has been demonstrated in two different cases. One being using a technique called DFT+μ (density functional theory with an included muon), in which a calculation is performed of the total energy of a supercell **[G]** of the structure to be modelled, but containing a muon located at a trial site[219,220]. The positions of the atoms in the supercell are then relaxed so that the muon can move and nearby ions distort[221]. If this is carried out with a large number of initial trial sites (and various schemes exist for efficiently sorting through the results [222]) then the lowest energy site can be identified, as well as quantifying the associated muon-induced distortions[219,220].

The distortions induced by the muon can sometimes have rather dramatic consequences: one notable example is found in Pr-based pyrochlores in which the muon-induced distortion affects the crystal field level of the Pr^{3+} ions and splits a non-Kramers doublet ground state (see **Error! Reference source not found.**9). This allows the new singlet ground state to couple to the nuclear degrees of freedom, thereby producing a very large nuclear relaxation of the muon spin that dominates the muon

response[223]. The DFT+μ technique has now been applied to a very wide range of materials, including inorganic[224] and molecular magnets [225], as well as materials hosting skyrmion ground states[226]. In addition, the methods have been extended to consider hyperfine fields in metals [227] and quantum effects [228] associated with the muon site that can be important due to the muon's small mass.

The other DFT based technique uses an Ab Initio Random Structure Search (AIRSS), to locate the muon[229]. The approach relies on providing information on the crystal structure of the system and through a series of random structure generation, the muon stopping sites can be solved. This approach was then extended to organic based samples where muonium interactions dominate, using Density Functional Tight Binding (DFTB), although this is not a true ab initio technique. The approach was able to show agreement with previously observed results from the organic molecules; durene, TCNQ and bithiophene. Finally, the pymuon suite[230] that uses an approached known as Unperturbed Electrostatic Potential, working mainly for muons within a diamagnetic environment. This approach uses a distribution of ions, with a positively charged nuclei and negatively charged electronic cloud, to compute the Coulomb potential at the muon site. This points to the interaction of the muon with the surrounding atoms to be very much a chemical problem that can be applied to a whole host of different systems.

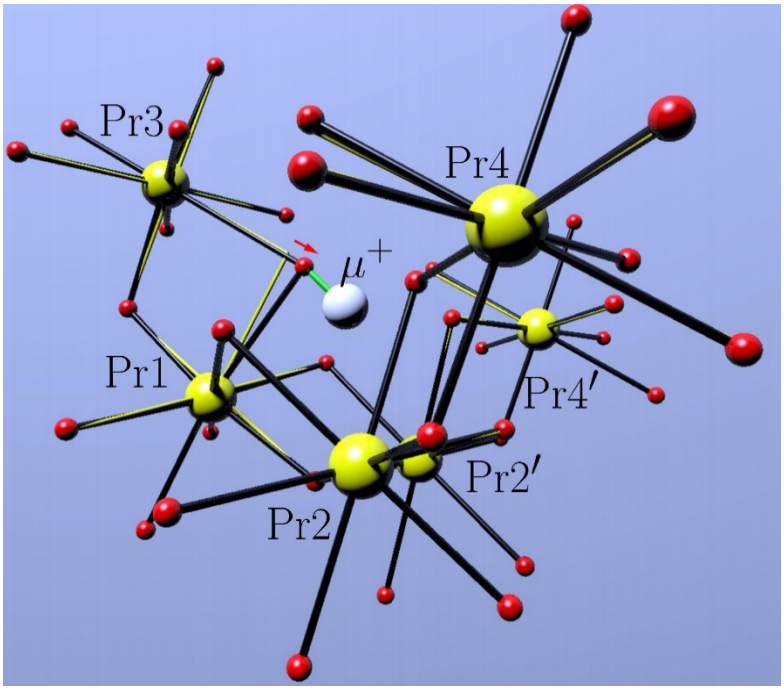

Figure 9: The calculated muon site in $Pr_2Sn_2O_7$, illustrating the local distortion induced by the presence of the muon. (After Ref. [223]).

In summary, muon spin relaxation and rotation (μSR) is an extremely powerful technique that yields useful and unique information to greatly enhance the understanding of topical and interesting materials. This primer on muon spin spectroscopy has provided an overview of the broad science program undertaken at muon facilities around the world. It is intended as a general introduction to the technique and highlights some of the particular successes that muon spin spectroscopy has had

over the years. Recently, there have been a number of excellent textbooks published, or at the time of writing this primer about to be published, that give more detailed information should it be required[6,8,13].

Glossary terms:

Abstraction reaction: Generally associated with hydrogen, where one hydrogen is able to abstract another from a system. In the case of muonium, the muon will abstract a hydrogen from a molecule resulting in a bond between the muonium and the molecule in question and a hydrogen atom (radical).

Auger electrons: An Auger electron results from the response of an atomic shell with a core vacancy induced by an external (electron or photon) excitation. This is namely the electron released from the outer shell of the excited atom while another outer shell electron relaxes to the core vacancy.

Cascade transition rates: time taken for a negative muon to cascade between specific energy levels.

Cyclotron: A particle accelerator that operates by accelerating charged particles with static magnetic fields and high frequency (RF) electric field. Cyclotrons tend to produce particles quasi-continuously, which results in, almost, a continuous source of muons.

Gyromagnetic ratio: The ratio of a particle's magnetic moment to its angular momentum, for a muon, the gyromagnetic ratio is = 2*pi x 135.5 MHz/T

Helicity: The projection of the spin of a particle onto the direction of momentum. The helicity is right-handed if the direction of its spin is the same as the direction of its motion and left-handed if it is opposite.

High-dilution limit: The limit approached when the muon is in extreme dilution. In this case, there are no muon-muon interactions due to the scarcity of the muon.

Hyperfine structure: Small shift and/or splitting of the energy levels caused by interactions between the nucleus and the electron clouds (known as hyperfine interactions).

K_α L_α, M_α energies: The energy of the X-ray when undergoing a transition between different atomic energy levels.

Kicked: When a muon, or pulse of muons, are sent down different beamlines by using either a magnetic or electrostatic force "kicking" the particles by a determined angle.

Larmor radius: The radius of the track of a charged particle in a magnetic field.

Longitudinal relaxation: The depolarisation of the muon spin along the longitudinal or z-direction, parallel to the initial muon spin.

Lorentz force: A force on a point charge from a combination of both electric and magnetic fields.

Momentum slits: Slits that allow particles through with a particular momentum. Often used in conjunction with a separator to ensure that only muons enter the instruments.

Muon cascade probability: The probability of a particular transition between specific energy levels occurring.

Muon hyperfine coupling constant: strength of interaction between the magnetic moments of the muon and an unpaired electron

Muon neutrinos: A neutrino is fundamental particles that have no charge, and the rest mass is small. For a long time it was the mass was thought to be zero, where actually the mass is <0.120 eV (<2.14 $x10^{-37}$kg). The neutrino only interacts with the weak interaction and gravity. The range of the weak interaction is short and as a neutrino do not interact via the strong interaction it will, typically, pass through matter with detection or interactions. The term muon neutrino refers to a neutrino that are produced during the decay process of a muon.

Muoniated radical: a radical formed from muonium addition to a double bond

Muonic atom: When a single negative muon is captured and bound to an atom.

Muonium: Muonium is a 'atom' formed of a positive muon and an electron. It is analogous to hydrogen, with a very similar electronic structure but only $1/9^{th}$ of its mass.

Nuclear capture: A nucleus of an atom can capture a muon (μ-) after cascading down the muonic atom energy levels.

Nuclear hyperfine coupling constants: strength of interaction between the magnetic moments of a nucleus and an unpaired electron. Only occurs for nuclei with non-zero spin.

Pions π: A particle (either positively, neutral or negative charged) that decays into a muon and muon neutrinos.

Precess: The response of a particle with spin in a magnetic field that is off-axis to the initial polarisation. The relative orientation of the particles spin changes in response to the magnetic field, where the precession can be visualised by picturing a spinning gyroscope.

Quadrupole magnets: A magnet with four pole pieces, generally used, in doublets or triplets, for focusing of a charged particle beam.

Separator: Two electrically charged plates and a dipole magnet with tuned electric and magnetic fields to act as a Wein filter. Often used in conjunction with momentum slits to ensure that only muons enter the instruments.

Soft error: An error (maybe temporary) in electronics where a bit has been changed, by an external source. This generally occurs through some interaction with particles and/or radiation.

Spin-polarised: The degree to which the spins are aligned along a particular direction.

Supercell: A large cell, generally associated with computation calculations, that are made up of many unit cells of the crystal structure.

Synchrotron: A particle accelerator that operates by accelerating charged in a closed loop where magnetic fields are used in a specific synchronised timing. To increase the kinetic energy of a bunch of particles RF fields are used. Synchrotrons produce high energy particles in short well defined bunches. This results in a pulsed source of muons

Thermalise: A process in which results in the physical properties reach thermal equilibrium.

Time resolution: The time that you can map in temporal space with a specific technique.

Time-differential measurements: A measurement probing how the muon polarisation evolves with time.

Time-integral measurements: the integrated polarisation of the muon is measured as a function of some external parameter, such as the applied magnetic field or the RF frequency, which are scanned in a series of steps.

Zero-point vibrational energy: The lowest energy state observed within a quantum mechanical system.

Acknowledgements

All authors acknowledge the support and access of the muons facilities around the world. In particular, the staff scientists and technical support teams over the years.

F. Bert acknowledges the support of the French Agence Nationale de la Recherche, under Grant No. ANR-18-CE30-0022

I. McKenzie acknowledges the support of a Discovery Grant from the Natural Sciences and Engineering Research Council of Canada.

A.D. Hillier acknowledges the support of an ERC grant (RACOM)

Author contributions

Introduction (A.H); Experimentation (A.B., K.S., I.M.K., T.P., I.W., A.H.); Results (K.S., I.M.K., A.H.); Applications (S.B., F.B., L.S., I.U., J.W., I.M.K., H.A., T.P., I.W., A.H.); Reproducibility and data deposition (A.H.); Limitations and optimizations (A.H., A.B.); Outlook (A.H., S.B., T.P.); All authors reviewed the content of the primer.

Competing interests

None

10 important references

*Hayano, R. S. et al. Zero-and low-field spin relaxation studied by positive muons. Physical Review B **20**, 850-859, doi:10.1103/PhysRevB.20.850 (1979)*

Comprehensive but concise and still actual description of the relaxations in zero and transverse field. The principle of the technics and the standard relaxation function are introduced.

*Cox, S. F. J. et al. Experimental Confirmation of the Predicted Shallow Donor Hydrogen State in Zinc Oxide. Physical Review Letters **86**, 2601-2604, doi:10.1103/PhysRevLett.86.2601 (2001).*

For the pioneer contribution of MuSR to the understanding of the role of hydrogen in semiconductors, namely when it incorporates the lattice structure either in a bond-centre configuration or as a shallow donor.

*Roduner, E. Muons, soap, and drug delivery - an invitation to enter a new field of research. Physica B-Condensed Matter **326**, 19-24, doi:10.1016/s0921-4526(02)01568-5 (2003).*

Demostarting the potential advances for for ALC μSR

Sugiyama, J. et al. Li Diffusion in LixCoO2 Probed by Muon-Spin Spectroscopy. Physical Review Letters 103, 147601, doi:10.1103/PhysRevLett.103.147601 (2009).

A significant paper showing Li diffusion observed by muSR and opened the field of the application of energy materials to μSR

Mendels, P.et al.Quantum magnetism in the paratacamite family: Towards an ideal kagome lattice.Physical Review Letters98, 077204,doi:10.1103/PhysRevLett.98.077204 (2007)

μSR has an unparalleled sensitivity to magnetic fields. This specificity is used in this article to discard even weak magnetic freezing in the first kagome based quantum spin liquid candidate.

*Ghosh, S. K. et al. Recent progress on superconductors with time-reversal symmetry breaking. Journal of Physics-Condensed Matter **33**, 28, doi:10.1088/1361-648X/abaa06 (2021).*

Recent review on time-reversal symmetry breaking showing the impact of muon experiments in discovery and understanding of unconventional superconductors

Wilkinson, J. M. & Blundell, S. J. Information and Decoherence in a Muon-Fluorine Coupled System. Physical Review Letters 125, 087201, doi:10.1103/PhysRevLett.125.087201 (2020).

Demonstration of the use of muons to model fundamental decoherence effects in the solid state.

Bakule, P. & Morenzoni, E. Generation and applications of slow polarized muons. Contemporary Physics 45, 203-225, doi:10.1080/00107510410001676803 (2004)

Demonstrating low-energy muons

Amato, A. Heavy-fermion systems studied by mu SR technique. Reviews of Modern Physics 69, 1119-1179, doi:10.1103/RevModPhys.69.1119 (1997).

A review of the impact muons have had in the field of heavy fermion science.

Sonier, J. E., Brewer, J. H. & Kiefl, R. F. mu SR studies of the vortex state in type-II superconductors. Reviews of Modern Physics 72, 769-811, doi:10.1103/RevModPhys.72.769 (2000).

A superconductivity review on the impact of muons.

References

1 Anderson, C. D. & Neddermeyer, S. H. Cloud Chamber Observations of Cosmic Rays at 4300 Meters Elevation and Near Sea-Level. *Physical Review* **50**, 263-271, doi:10.1103/PhysRev.50.263 (1936).

2 Garwin, R. L., Lederman, L. M. & Weinrich, M. OBSERVATIONS OF THE FAILURE OF CONSERVATION OF PARITY AND CHARGE CONJUGATION IN MESON DECAYS - MAGNETIC MOMENT OF THE FREE MUON. *Physical Review* **105**, 1415-1417, doi:10.1103/PhysRev.105.1415 (1957).

3 Wulf, T. Über den Ursprung der in der Atmosphäre vorhandenen γ-Strahlung. *Phys. Z.* **10**, 811 (1909).

4 Hess, V. F. Über Beobachtungen der durchdringenden Strahlung bei sieben Freiballonfahrten. *Phys. Z* **13**, 1084 (1912).
5 Conversi, M., Pancini, E. & Piccioni, O. On the Decay Process of Positive and Negative Mesons. *Physical Review* **68**, 232, doi:10.1103/PhysRev.68.232 (1945).
6 Blundell, S., deRenzi, R., Lancaster, T. & Pratt, F. *Introduction to Muon Spectroscopy*. (Oxford University Press, 2021).
7 Schenck, A. *Muon Spin Rotation: Principles and Applications in Solid State Physics*. (Adam Hilger, 1985).
8 Yaouanc, A. & Dalmas de Réotier, P. *Muon Spin Rotation, Relaxation, and Resonance*. (Oxford University Press, 2010).
9 Nagamine, K. *Introductory Muon Science*. (Cambridge University Press, 2003).
10 **Roduner** , E. *The Positive Muon as a Probe in Free Radical Chemistry*. (Springer, 1988).
11 Lee, S. L., Kilcoyne, S. H. & Cywinski, R. *Muon science : muons in physics, chemistry and materials : proceedings of the fifty first Scottish universities summer school in physics, St Andrews, August 1998*. (1999).
12 Walker, D. C. *Muon and Muonium Chemistry*. (Cambridge University Press, 1983).
13 Morenzoni, E. & Amato, A. in *Lecture Notes in Physics* (Springer, 2022).
14 Matsuzaki, T. *et al.* The RIKEN-RAL pulsed Muon Facility. *Nuclear Instruments & Methods in Physics Research Section a-Accelerators Spectrometers Detectors and Associated Equipment* **465**, 365-383, doi:10.1016/s0168-9002(01)00694-5 (2001).
15 Hillier, A. D., Lord, J. S., Ishida, K. & Rogers, C. Muons at ISIS. *Philosophical Transactions of the Royal Society a-Mathematical Physical and Engineering Sciences* **377**, 7, doi:10.1098/rsta.2018.0064 (2019).
16 Instruments, P. *PSI Muon Web Page*, <https://www.psi.ch/en/smus/instruments> (
17 TRIUMF. *TRIUMF Muon Web Pages*, <http://cmms.triumf.ca/> (
18 Cook, S. *et al.* Delivering the world's most intense muon beam. *Physical Review Accelerators and Beams* **20**, 030101, doi:10.1103/PhysRevAccelBeams.20.030101 (2017).
19 Miyake, Y. *et al.* J-PARC Muon Facility, MUSE. *Physics Procedia* **30**, 46-49, doi:10.1016/j.phpro.2012.04.037 (2012).
20 Hillier, A. D. *et al.* Developments at the ISIS muon source and the concomitant benefit to the user community. *Journal of Physics Conference Series* **551**, 012067, doi:10.1088/1742-6596/551/1/012067 (2014).
21 Giblin, S. R. *et al.* Optimising a muon spectrometer for measurements at the ISIS pulsed muon source. *Nuclear Instruments & Methods in Physics Research Section a-Accelerators Spectrometers Detectors and Associated Equipment* **751**, 70-78, doi:10.1016/j.nima.2014.03.010 (2014).
22 Abela, R. *et al.* Muons on request (MORE): combining advantages of continuous and pulsed muon beams. *Hyperfine Interactions* **120**, 575-578, doi:10.1023/a:1017046817431 (1999).
23 Bakule, P. & Morenzoni, E. Generation and applications of slow polarized muons. *Contemp. Phys.* **45**, 203-225, doi:10.1080/00107510410001676803 (2004).
24 Pant, A. D. *et al.* Characterization and optimization of ultra slow muon beam at J-PARC/MUSE: A simulation study. *Nuclear Instruments & Methods in Physics Research Section a-Accelerators Spectrometers Detectors and Associated Equipment* **929**, 129-133, doi:10.1016/j.nima.2019.02.065 (2019).
25 Nakamura, J. *et al.* Ultra Slow Muon Microscope at MUSE / J-PARC. *Journal of Physics: Conference Series* **502**, 012042, doi:10.1088/1742-6596/502/1/012042 (2014).
26 Miyake, Y. *et al.* Ultra Slow Muon Project at J-PARC MUSE. *Journal of the Physical Society of Japan* **2**, 010101, doi:10.7566/JPSCP.2.010101 (2014).
27 Prokscha, T. *et al.* The new mu E4 beam at PSI: A hybrid-type large acceptance channel for the generation of a high intensity surface-muon beam. *Nuclear Instruments & Methods in*

Physics Research Section a-Accelerators Spectrometers Detectors and Associated Equipment **595**, 317-331, doi:10.1016/j.nima.2008.07.081 (2008).

28 Morenzoni, E., Prokscha, T., Suter, A., Luetkens, H. & Khasanov, R. Nano-scale thin film investigations with slow polarized muons. *Journal of Physics-Condensed Matter* **16**, S4583-S4601, doi:10.1088/0953-8984/16/40/010 (2004).

29 Khasanov, R. *et al.* High pressure research using muons at the Paul Scherrer Institute. *High Pressure Res.* **36**, 140-166, doi:10.1080/08957959.2016.1173690 (2016).

30 Watanabe, I. *et al.* Development of a gas-pressurized high-pressure mu SR setup at the RIKEN-RAL Muon Facility. *Physica B-Condensed Matter* **404**, 993-995, doi:10.1016/j.physb.2008.11.209 (2009).

31 Hillier, A. D., Cottrell, S. P., King, P. J. C., Eaton, G. H. & Clarke-Gayther, M. A. High frequency measurements at a pulsed muon source: beating the pulse width! *Physica B-Condensed Matter* **326**, 275-278, doi:10.1016/s0921-4526(02)01629-0 (2003).

32 Cottrell, S. P., Johnson, C., Cox, S. F. J. & Scott, C. A. Radio-frequency techniques for muon charge state conversion measurements. *Physica B-Condensed Matter* **326**, 248-251, doi:10.1016/s0921-4526(02)01616-2 (2003).

33 Fleming, D. G., Cottrell, S. P., McKenzie, I. & Ghandi, K. Rate constants for the slow Mu plus propane abstraction reaction at 300 K by diamagnetic RF resonance. *Physical Chemistry Chemical Physics* **17**, 19901-19910, doi:10.1039/c5cp02576a (2015).

34 Kadono, R., Matsushita, A., Macrae, R. M., Nishiyama, K. & Nagamine, K. MUONIUM CENTERS IN CRYSTALLINE SI AND GE UNDER ILLUMINATION. *Physical Review Letters* **73**, 2724-2727, doi:10.1103/PhysRevLett.73.2724 (1994).

35 Yokoyama, K. *et al.* The new high field photoexcitation muon spectrometer at the ISIS pulsed neutron and muon source. *Review of Scientific Instruments* **87**, 12511, doi:10.1063/1.4972827 (2016).

36 Prokscha, T., Chow, K. H., Salman, Z., Stilp, E. & Suter, A. Direct Observation of Hole Carrier-Density Profiles and Their Light-Induced Manipulation at the Surface of Ge. *Physical Review Applied* **14**, 014098, doi:10.1103/PhysRevApplied.14.014098 (2020).

37 Eshchenko, D. G., Storchak, V. G., Cottrell, S. P. & Morenzoni, E. Electric-Field-Enhanced Neutralization of Deep Centers in GaAs. *Physical Review Letters* **103**, 216601, doi:10.1103/PhysRevLett.103.216601 (2009).

38 Hampshire, B. V. *et al.* Using Negative Muons as a Probe for Depth Profiling Silver Roman Coinage. *Heritage* **2**, doi:10.3390/heritage2010028 (2019).

39 Hillier, A. D., Paul, D. M. & Ishida, K. Probing beneath the surface without a scratch Bulk non-destructive elemental analysis using negative muons. *Microchemical Journal* **125**, 203-207, doi:10.1016/j.microc.2015.11.031 (2016).

40 Clemenza, M. *et al.* Muonic atom X-ray spectroscopy for non-destructive analysis of archeological samples. *Journal of Radioanalytical and Nuclear Chemistry* **322**, 1357-1363, doi:10.1007/s10967-019-06927-6 (2019).

41 A. Hillier, K. I., P. Seller, M. C. Veale, M. D. Wilson. Element Specific Imaging Using Muonic X-rays. *JPS Conf. Proc.* **21**, 011042 (2018).

42 G. Yabu, M. K., M. Tampo, K. Hamada, A. Harayama, Y. Miyake, S. Oshita, S. Saito, G. Sato, T. Takahashi, S. Takeda, S. Watanabe. Imaging of Muonic X-ray of Light Elements with a CdTe Double-Sided Strip Detector. *JPS Conf. Series* **21**, 011044 (2018).

43 NIST. *The NIST Reference on Constants, Units, and Uncertainty.*, <http://physics.nist.gov/cuu/Constants/index.html> (

44 Hayano, R. S. *et al.* Zero-and low-field spin relaxation studied by positive muons. *Physical Review B* **20**, 850-859, doi:10.1103/PhysRevB.20.850 (1979).

45 Rainford, B. D. & Daniell, G. J. MU-SR FREQUENCY-SPECTRA USING THE MAXIMUM-ENTROPY METHOD. *Hyperfine Interactions* **87**, 1129-1134, doi:10.1007/bf02068515 (1994).

46 Gil, J. M. *et al.* Novel Muonium State in CdS. *Physical Review Letters* **83**, 5294-5297, doi:10.1103/PhysRevLett.83.5294 (1999).
47 McKenzie, I. The positive muon and μSR spectroscopy: powerful tools for investigating the structure and dynamics of free radicals and spin probes in complex systems. *Annual Reports Section "C" (Physical Chemistry)* **109**, 65-112, doi:10.1039/c3pc90005c (2013).
48 Heming, M. *et al.* DETECTION OF MUONATED FREE-RADICALS THROUGH THE EFFECTS OF AVOIDED LEVEL-CROSSING - THEORY AND ANALYSIS OF SPECTRA. *Chemical Physics Letters* **128**, 100-106, doi:10.1016/0009-2614(86)80154-3 (1986).
49 Percival, P. W. *et al.* C-13 HYPERFINE COUPLING-CONSTANTS IN MUC(60). *Chemical Physics Letters* **245**, 90-94, doi:10.1016/0009-2614(95)00951-y (1995).
50 McKenzie, I., Scheuermann, R. & Sedlak, K. How Do Strain and Steric Interactions Affect the Reactions of Aromatic Compounds with Free Radicals? Characterization of the Radicals Formed by Muonium Addition to p-Xylene and 2.2 Paracyclophane by DFT Calculations and Muon Spin Spectroscopy. *J. Phys. Chem. A* **116**, 7765-7772, doi:10.1021/jp305610g (2012).
51 Roduner, E., Reid, I. D., Ricco, M. & De Renzi, R. ANISOTROPY OF 2-NORBORNYL RADICAL REORIENTATIONAL DYNAMICS IN THE PLASTIC PHASE OF NORBORNENE AS DETERMINED BY ALC-MU-SR. *Ber. Bunsen-Ges. Phys. Chem. Chem. Phys.* **93**, 1194-1197, doi:10.1002/bbpc.19890931109 (1989).
52 Measday, D. F. The nuclear physics of muon capture. *Physics Reports-Review Section of Physics Letters* **354**, 243-409, doi:10.1016/s0370-1573(01)00012-6 (2001).
53 K. NINOMIYA, M. K. K., P. STRASSER, A. SHINOHARA, M. TAMPO, N. KAWAMURA, Y. MIYAKE. Isotope identification of lead by muon induced X-ray and gamma-ray measurements. *JPS. Conf. Proc.* **21**, 011043 (2018).
54 Suter, A. & Wojek, B. M. musrfit: a free platform-independent framework for mu SR data analysis. *12th International Conference on Muon Spin Rotation, Relaxation and Resonance (Musr2011)* **30**, 69-73, doi:10.1016/j.phpro.2012.04.042 (2012).
55 Pratt, F. L. WIMDA: a muon data analysis program for the Windows PC. *Physica B* **289**, 710-714, doi:10.1016/s0921-4526(00)00328-8 (2000).
56 Mantid. *Mantid Project Website*, <https://www.mantidproject.org/Main_Page> (2020).
57 Baker, P. J., Loe, T., Telling, M., Cottrell, S. P. & Hillier, A. D. in *Proceedings of the 14th International Conference on Muon Spin Rotation, Relaxation and Resonance (?SR2017)* Vol. 21 *JPS Conference Proceedings* (Journal of the Physical Society of Japan, 2018).
58 Luetkens, H. *et al.* The electronic phase diagram of the LaO1-xFxFeAs superconductor. *Nat. Mater.* **8**, 305-309, doi:10.1038/nmat2397 (2009).
59 Drew, A. J. *et al.* Coexistence of static magnetism and superconductivity in SmFeAsO1-xFx as revealed by muon spin rotation. *Nat. Mater.* **8**, 310-314, doi:10.1038/nmat2396 (2009).
60 Parker, D. R. *et al.* Control of the Competition between a Magnetic Phase and a Superconducting Phase in Cobalt-Doped and Nickel-Doped NaFeAs Using Electron Count. *Physical Review Letters* **104**, 057007, doi:10.1103/PhysRevLett.104.057007 (2010).
61 Hayward, M. A. *et al.* The hydride anion in an extended transition metal oxide array: LaSrCoO3H0.7. *Science* **295**, 1882-1884, doi:10.1126/science.1068321 (2002).
62 Campbell, I. A. *et al.* DYNAMICS IN CANONICAL SPIN-GLASSES OBSERVED BY MUON SPIN DEPOLARIZATION. *Physical Review Letters* **72**, 1291-1294, doi:10.1103/PhysRevLett.72.1291 (1994).
63 Lovesey, S. W., Trohidou, K. N. & Karlsson, E. B. MUON SPIN RELAXATION IN FERROMAGNETS .2. CRITICAL AND PARAMAGNETIC MAGNETIZATION FLUCTUATIONS. *Journal of Physics-Condensed Matter* **4**, 2061-2071, doi:10.1088/0953-8984/4/8/019 (1992).
64 Uemura, Y. J. *et al.* Phase separation and suppression of critical dynamics at quantum phase transitions of MnSi and (Sr1-xCax)RuO3. *Nat. Phys.* **3**, 29-35, doi:10.1038/nphys488 (2007).
65 Uemura, Y. J., Harshman, D. R., Senba, M., Ansaldo, E. J. & Murani, A. P. Zero-field muon-spin relaxation in $\mathrm{Cu} \mathrm{Mn}$ spin-glasses compared with neutron and

susceptibility experiments. *Physical Review B* **30**, 1606-1608, doi:10.1103/PhysRevB.30.1606 (1984).
66 Yaouanc, A., Dereotier, P. D. & Frey, E. ZERO-FIELD MUON-SPIN-RELAXATION DEPOLARIZATION RATE OF PARAMAGNETS NEAR THE CURIE-TEMPERATURE. *Physical Review B* **47**, 796-809, doi:10.1103/PhysRevB.47.796 (1993).
67 Pratt, F. *et al.* Muon spin relaxation studies of critical fluctuations and diffusive spin dynamics in molecular magnets. *Physica B: Condensed Matter* **404**, 585-589, doi:https://doi.org/10.1016/j.physb.2008.11.123 (2009).
68 Berlie, A., Terry, I. & Szablewski, M. A 3D antiferromagnetic ground state in a quasi-1D π-stacked charge-transfer system. *Journal of Materials Chemistry C* **6**, 12468-12472, doi:10.1039/C8TC03709D (2018).
69 Adroja, D. T. *et al.* Muon spin rotation and neutron scattering investigations of the B-site ordered double perovskite Sr2DyRuO6. *Physical Review B* **101**, 13, doi:10.1103/PhysRevB.101.094413 (2020).
70 Yamauchi, H. *et al.* High-temperature short-range order in Mn3RhSi. *Communications Materials* **1**, 43, doi:10.1038/s43246-020-0042-1 (2020).
71 Dally, R. *et al.* Short-Range Correlations in the Magnetic Ground State of ${\mathrm{Na}}_{4}{\mathrm{Ir}}_{3}{\mathrm{O}}_{8}$. *Physical Review Letters* **113**, 247601, doi:10.1103/PhysRevLett.113.247601 (2014).
72 Rainford, B. D., Cywinski, R. & Dakin, S. J. NEUTRON AND MU-SR STUDIES OF SPIN FLUCTUATIONS IN YMN2 AND RELATED ALLOYS. *Journal of Magnetism and Magnetic Materials* **140**, 805-806, doi:10.1016/0304-8853(94)00681-4 (1995).
73 Le, L. P. *et al.* SEARCHING FOR SPONTANEOUS MAGNETIC ORDER IN AN ORGANIC FERROMAGNET - MU-SR STUDIES OF BETA-PHASE P-NPNN. *Chemical Physics Letters* **206**, 405-408, doi:10.1016/0009-2614(93)85573-7 (1993).
74 Blundell, S. J. *et al.* MU(+) SR OF THE ORGANIC FERROMAGNET P-NPNN - DIAMAGNETIC AND PARAMAGNETIC STATES. *Europhys. Lett.* **31**, 573-578, doi:10.1209/0295-5075/31/9/012 (1995).
75 Kojima, K. M. *et al.* Reduction of ordered moment and Neel temperature of quasi-one-dimensional antiferromagnets Sr2CuO3 and Ca2CuO3. *Physical Review Letters* **78**, 1787-1790, doi:10.1103/PhysRevLett.78.1787 (1997).
76 Sengupta, P., Sandvik, A. W. & Singh, R. R. P. Specific heat of quasi-two-dimensional antiferromagnetic Heisenberg models with varying interplanar couplings. *Physical Review B* **68**, 7, doi:10.1103/PhysRevB.68.094423 (2003).
77 Lancaster, T. *et al.* Magnetic order in the quasi-one-dimensional spin- 1∕2 molecular chain compound copper pyrazine dinitrate. *Physical Review B* **73**, 020410, doi:10.1103/PhysRevB.73.020410 (2006).
78 Pratt, F. L., Blundell, S. J., Lancaster, T., Baines, C. & Takagi, S. Low-temperature spin diffusion in a highly ideal S=1/2 Heisenberg antiferromagnetic chain studied by Muon spin relaxation. *Physical Review Letters* **96**, 247203, doi:10.1103/PhysRevLett.96.247203 (2006).
79 Manson, J. L. *et al.* Ag(nic)(2) (nic = Nicotinate): A Spin-Canted Quasi-2D Antiferromagnet Composed of Square-Planar S=1/2 Ag-II Ions. *Inorg. Chem.* **51**, 1989-1991, doi:10.1021/ic202600n (2012).
80 Lancaster, T. *et al.* Quantum magnetism in molecular spin ladders probed with muonspin spectroscopy. *New J. Phys.* **20**, 103002, doi:10.1088/1367-2630/aae21a (2018).
81 Pratt, F. Superconductivity and Magnetism in Organic Materials Studied with mu SR. *Journal of the Physical Society of Japan* **85**, 091008, doi:10.7566/jpsj.85.091008 (2016).
82 Manson, J. L. *et al.* Cu(HF2)(pyz)(2) BF4 (pyz=pyrazine): long-range magnetic ordering in a pseudo-cubic coordination polymer comprised of bridging HF2- and pyrazine ligands. *Chem. Commun.*, 4894-4896, doi:10.1039/b608791d (2006).

83 Mendels, P. *et al.* Quantum magnetism in the paratacamite family: Towards an ideal kagome lattice. *Physical Review Letters* **98**, 077204, doi:10.1103/PhysRevLett.98.077204 (2007).

84 Amato, A. *et al.* Understanding the mu SR spectra of MnSi without magnetic polarons. *Physical Review B* **89**, 184425, doi:10.1103/PhysRevB.89.184425 (2014).

85 Wang, R. Z. *et al.* Quantum Griffiths Phase Inside the Ferromagnetic Phase of Ni1-xVx. *Physical Review Letters* **118**, 267202, doi:10.1103/PhysRevLett.118.267202 (2017).

86 Frandsen, B. A. *et al.* Volume-wise destruction of the antiferromagnetic Mott insulating state through quantum tuning. *Nat. Commun.* **7**, 12519, doi:10.1038/ncomms12519 (2016).

87 Kirschner, F. K. K. *et al.* Spin Jahn-Teller antiferromagnetism in CoTi2O5. *Physical Review B* **99**, 064403, doi:10.1103/PhysRevB.99.064403 (2019).

88 Pratt, F. L. *et al.* Magnetic and non-magnetic phases of a quantum spin liquid. *Nature* **471**, 612-616, doi:10.1038/nature09910 (2011).

89 Yaouanc, A. *et al.* Dynamical Splayed Ferromagnetic Ground State in the Quantum Spin Ice Yb2Sn2O7. *Physical Review Letters* **110**, 127207, doi:10.1103/PhysRevLett.110.127207 (2013).

90 Kirschner, F. K. K., Flicker, F., Yacoby, A., Yao, N. Y. & Blundell, S. J. Proposal for the detection of magnetic monopoles in spin ice via nanoscale magnetometry. *Physical Review B* **97**, 140402(R), doi:10.1103/PhysRevB.97.140402 (2018).

91 Brewer, J. H. *et al.* OBSERVATION OF MUON-FLUORINE HYDROGEN-BONDING IN IONIC-CRYSTALS. *Physical Review B* **33**, 7813-7816, doi:10.1103/PhysRevB.33.7813 (1986).

92 Lancaster, T. *et al.* Muon-fluorine entangled states in molecular magnets. *Physical Review Letters* **99**, 267601, doi:10.1103/PhysRevLett.99.267601 (2007).

93 Wilkinson, J. M. & Blundell, S. J. Information and Decoherence in a Muon-Fluorine Coupled System. *Physical Review Letters* **125**, 087201, doi:10.1103/PhysRevLett.125.087201 (2020).

94 Aidoudi, F. H. *et al.* An ionothermally prepared S=1/2 vanadium oxyfluoride kagome lattice. *Nature Chemistry* **3**, 801-806, doi:10.1038/nchem.1129 (2011).

95 Abdeldaim, A. H. *et al.* Realizing square and diamond lattice S=1/2 Heisenberg antiferromagnet models in the alpha and beta phases of the coordination framework, KTi(C2O4)(2)center dot xH(2)O. *Physical Review Materials* **4**, doi:10.1103/PhysRevMaterials.4.104414 (2020).

96 Majumder, M. *et al.* Breakdown of Magnetic Order in the Pressurized Kitaev Iridate β-Li2IrO3. *Physical Review Letters* **120**, 237202-237202, doi:10.1103/PhysRevLett.120.237202 (2018).

97 Li, Y. *et al.* Muon Spin Relaxation Evidence for the U(1) Quantum Spin-Liquid Ground State in the Triangular Antiferromagnet YbMgGaO4. *Physical Review Letters* **117**, 97201-97201, doi:10.1103/PhysRevLett.117.097201 (2016).

98 Colman, R. H. *et al.* Spin dynamics in the S=1/2 quantum kagome compound vesignieite, Cu3Ba(VO5H)(2). *Physical Review B* **83**, 180416, doi:10.1103/PhysRevB.83.180416 (2011).

99 Pratt, F. L. Probing Quantum Critical Spin Liquids with uSR. *JPS Conference Proceedings* **21**, 011002, doi:10.7566/JPSCP.21.011002 (2018).

100 Gomilšek, M. *et al.* Kondo screening in a charge-insulating spinon metal. *Nat. Phys.* **15**, 754-758, doi:10.1038/s41567-019-0536-2 (2019).

101 Amato, A. Heavy-fermion systems studied by mu SR technique. *Reviews of Modern Physics* **69**, 1119-1179, doi:10.1103/RevModPhys.69.1119 (1997).

102 Sonier, J. E., Brewer, J. H. & Kiefl, R. F. mu SR studies of the vortex state in type-II superconductors. *Reviews of Modern Physics* **72**, 769-811, doi:10.1103/RevModPhys.72.769 (2000).

103 Tinkham, M. *Introduction to Superconductivity*. Second Edition edn, (McGraw Hill, 1996).

104 Sonier, J. E. mu SR Studies of Cuprate Superconductors. *Journal of the Physical Society of Japan* **85**, 091005, doi:10.7566/jpsj.85.091005 (2016).

105 Khasanov, R. *et al.* Two-Gap Superconductivity in Ba1-xKxFe2As2: A Complementary Study of the Magnetic Penetration Depth by Muon-Spin Rotation and Angle-Resolved Photoemission. *Physical Review Letters* **102**, 187005, doi:10.1103/PhysRevLett.102.187005 (2009).
106 Uemura, Y. J. Dynamic superconductivity responses in photoexcited optical conductivity and Nernst effect. *Physical Review Materials* **3**, 104801, doi:10.1103/PhysRevMaterials.3.104801 (2019).
107 Uemura, Y. J. *et al.* MAGNETIC-FIELD PENETRATION DEPTH IN TL2BA2CUO6+DELTA IN THE OVERDOPED REGIME. *Nature* **364**, 605-607, doi:10.1038/364605a0 (1993).
108 Sigrist, M. & Ueda, K. PHENOMENOLOGICAL THEORY OF UNCONVENTIONAL SUPERCONDUCTIVITY. *Reviews of Modern Physics* **63**, 239-311, doi:10.1103/RevModPhys.63.239 (1991).
109 Schenck, A. in *Muon Science: Muons in Physics, Chemistry and Materials.Muon Science: Muons in Physics, Chemistry and Materials.* (eds SL Lee, R Cywinski, & SH Kilcoyne) (Institute of Physics, 1999).
110 Luke, G. M. *et al.* Time-reversal symmetry breaking superconductivity in Sr2RuO4. *Nature* **394**, 558-561, doi:10.1038/29038 (1998).
111 Hillier, A. D., Quintanilla, J. & Cywinski, R. Evidence for Time-Reversal Symmetry Breaking in the Noncentrosymmetric Superconductor LaNiC2. *Physical Review Letters* **102**, 117007, doi:10.1103/PhysRevLett.105.229901 (2010).
112 Aoki, Y. *et al.* Time-reversal symmetry-breaking superconductivity in heavy-fermion PrOs(4)Sb(12) detected by muon-spin relaxation. *Physical Review Letters* **91**, 067003, doi:10.1103/PhysRevLett.91.067003 (2003).
113 Maisuradze, A. *et al.* Evidence for time-reversal symmetry breaking in superconducting PrPt4Ge12. *Physical Review B* **82**, 024524, doi:10.1103/PhysRevB.82.024524 (2010).
114 Ghosh, S. K. *et al.* Recent progress on superconductors with time-reversal symmetry breaking. *Journal of Physics-Condensed Matter* **33**, 28, doi:10.1088/1361-648X/abaa06 (2021).
115 Adachi, T. *et al.* Muon spin relaxation and magnetic susceptibility studies of the effects of nonmagnetic impurities on the Cu spin dynamics and superconductivity in La2-xSrxCu1-yZnyO4 around x=0.115. *Physical Review B* **69**, 184507, doi:10.1103/PhysRevB.69.184507 (2004).
116 Zhang, J. *et al.* Discovery of slow magnetic fluctuations and critical slowing down in the pseudogap phase of YBa2Cu3Oy. *Science Advances* **4**, eaao5235, doi:10.1126/sciadv.aao5235 (2018).
117 Kaiser, C. T. *et al.* Li mobility in the battery cathode material Li-x Mn1.96Li0.04 O-4 studied by muon-spin relaxation. *Physical Review B* **62**, R9236-R9239, doi:10.1103/PhysRevB.62.R9236 (2000).
118 Ariza, M. J., Jones, D. J., Roziere, J., Lord, J. S. & Ravot, D. Muon spin relaxation study of spinel lithium manganese oxides. *J. Phys. Chem. B* **107**, 6003-6011, doi:10.1021/jp027022n (2003).
119 Sugiyama, J. *et al.* Li Diffusion in LixCoO2 Probed by Muon-Spin Spectroscopy. *Physical Review Letters* **103**, 147601, doi:10.1103/PhysRevLett.103.147601 (2009).
120 Sugiyama, J. *et al.* Reactive surface area of the Lix(Co1/3Ni1/3Mn1/3)O2 electrode determined by μ+SR and electrochemical measurements. *Physical Chemistry Chemical Physics* **15**, 10402-10412, doi:10.1039/c3cp51662h (2013).
121 Sugiyama, J. *et al.* Low-temperature magnetic properties and high-temperature diffusive behavior of LiNiO2 investigated by muon-spin spectroscopy. *Physical Review B* **82**, 224412, doi:10.1103/PhysRevB.82.224412 (2010).
122 Sugiyama, J. *et al.* Magnetic and diffusive nature of LiFePO4 investigated by muon spin rotation and relaxation. *Physical Review B* **84**, 054430, doi:10.1103/PhysRevB.84.054430 (2011).

123 Sugiyama, J. *et al.* Diffusive behavior in LiMPO4 with M = Fe, Co, Ni probed by muon-spin relaxation. *Physical Review B* **85**, 054111, doi:10.1103/PhysRevB.85.054111 (2012).
124 Sugiyama, J. *et al.* Antiferromagnetic spin structure and lithium ion diffusion in Li2MnO3 probed by mu+SR. *Physical Review B* **87**, 024409, doi:10.1103/PhysRevB.87.024409 (2013).
125 Sugiyama, J. *et al.* Li-ion diffusion in Li4Ti5O12 and LiTi2O4 battery materials detected by muon spin spectroscopy. *Physical Review B* **92**, 014417, doi:10.1103/PhysRevB.92.014417 (2015).
126 Sugiyama, J. *et al.* Lithium diffusion in spinel Li4Ti5O12 and LiTi2O4 films detected with Li-8 beta-NMR. *Physical Review B* **96**, 094402, doi:10.1103/PhysRevB.96.094402 (2017).
127 Powell, A. S., Lord, J. S., Gregory, D. H. & Titman, J. J. Muon Spin Relaxation Studies of Lithium Nitridometallate Battery Materials: Muon Trapping and Lithium Ion Diffusion. *J. Phys. Chem. C* **113**, 20758-20763, doi:10.1021/jp9091249 (2009).
128 Powell, A. S. *et al.* Insight into lithium transport in lithium nitridometallate battery materials from muon spin relaxation. *Physical Chemistry Chemical Physics* **15**, 816-823, doi:10.1039/c2cp43318d (2013).
129 Baker, P. J. *et al.* Probing magnetic order in LiMPO4 (M = Ni, Co, Fe) and lithium diffusion in LixFePO4. *Physical Review B* **84**, 174403, doi:10.1103/PhysRevB.84.174403 (2011).
130 Johnson, I. D. *et al.* Mechanistic insights of Li+ diffusion within doped LiFePO4 from Muon Spectroscopy. *Scientific Reports* **8**, 4114, doi:10.1038/s41598-018-22435-1 (2018).
131 Ashton, T. E. *et al.* Multiple diffusion pathways in LixNi0.77Co0.14Al0.09O2(NCA) Li-ion battery cathodes. *J. Mater. Chem. A* **8**, 11545-11552, doi:10.1039/d0ta03809a (2020).
132 Ashton, T. E. *et al.* Muon studies of Li+ diffusion in LiFePO4 nanoparticles of different polymorphs. *J. Mater. Chem. A* **2**, 6238-6245, doi:10.1039/c4ta00543k (2014).
133 Ashton, T. E. *et al.* Stoichiometrically driven disorder and local diffusion in NMC cathodes. *J. Mater. Chem. A* **9**, 10477-10486, doi:10.1039/d1ta01639c (2021).
134 Medarde, M. *et al.* 1D to 2D Na+ Ion Diffusion Inherently Linked to Structural Transitions in Na0.7CoO2. *Physical Review Letters* **110**, 266401, doi:10.1103/PhysRevLett.110.266401 (2013).
135 Mansson, M. & Sugiyama, J. Muon-spin relaxation study on Li- and Na-diffusion in solids. *Physica Scripta* **88**, 068509, doi:10.1088/0031-8949/88/06/068509 (2013).
136 Sugiyama, J. *et al.* Lithium diffusion in LiMnPO4 detected with mu+-SR. *Physical Review Research* **2**, 033161, doi:10.1103/PhysRevResearch.2.033161 (2020).
137 Umegaki, I. *et al.* Li-ion diffusion in Li intercalated graphite C6Li and C12Li probed by mu+SR. *Physical Chemistry Chemical Physics* **19**, 19058-19066, doi:10.1039/c7cp02047c (2017).
138 Umegaki, I. *et al.* Battery Materials Research with Muon Beam. *JPS Conference Proceedings* **25**, 011009, doi:doi:10.7566/JPSCP.25.011009 10.7566/JPSCP.25.011009 (2019).
139 McClelland, I. *et al.* in *Annual Review of Materials Research, Vol 50, 2020* Vol. 50 *Annual Review of Materials Research* (ed D. R. Clarke) 371-393 (Annual Reviews, 2020).
140 Kadono, R. *et al.* Hydrogen bonding in sodium alanate: A muon spin rotation study. *Physical Review Letters* **100**, 026401, doi:10.1103/PhysRevLett.100.026401 (2008).
141 Sugiyama, J. *et al.* Desorption reaction in MgH2 studied with in situ mu+SR. *Sustain. Energ. Fuels* **3**, 956-964, doi:10.1039/c8se00568k (2019).
142 Sugiyama, J. *et al.* Nuclear Magnetic Field in Solids Detected with Negative-Muon Spin Rotation and Relaxation. *Physical Review Letters* **121**, 087202, doi:10.1103/PhysRevLett.121.087202 (2018).
143 Roduner, E. *et al.* QUANTUM PHENOMENA AND SOLVENT EFFECTS ON ADDITION OF HYDROGEN ISOTOPES TO BENZENE AND TO DIMETHYLBUTADIENE. *Ber. Bunsen-Ges. Phys. Chem. Chem. Phys.* **94**, 1224-1230, doi:10.1002/bbpc.199000008 (1990).
144 Nicovich, J. M. & Ravishankara, A. R. REACTION OF HYDROGEN-ATOM WITH BENZENE - KINETICS AND MECHANISM. *J. Phys. Chem.* **88**, 2534-2541, doi:10.1021/j150656a021 (1984).

145 Mezyk, S. P. & Bartels, D. M. RATE-CONSTANT AND ACTIVATION-ENERGY MEASUREMENT FOR THE REACTION OF ATOMIC-HYDROGEN WITH METHANOL, IODOMETHANE, IODOETHANE, AND 1-IODOPROPANE IN AQUEOUS-SOLUTION. *J. Phys. Chem.* **98**, 10578-10583, doi:10.1021/j100092a031 (1994).
146 Ghandi, K. *et al.* Muonium kinetics in sub- and supercritical water. *Physica B-Condensed Matter* **326**, 55-60, doi:10.1016/s0921-4526(02)01572-7 (2003).
147 Percival, P. W., Brodovitch, J. C., Ghandi, K., McCollum, B. M. & McKenzie, I. H atom kinetics in superheated water studied by muon spin spectroscopy. *Radiat. Phys. Chem.* **76**, 1231-1235, doi:10.1016/j.radphyschem.2007.02.010 (2007).
148 Laidler, K. J. & Keith, J. *Chemical Kinetics*. (Harper & Row, 1987).
149 Chandrasena, L. *et al.* Free Radical Reactivity of a Phosphaalkene Explored Through Studies of Radical Isotopologues. *Angewandte Chemie International Edition* **58**, 297-301, doi:https://doi.org/10.1002/anie.201810967 (2019).
150 Scheuermann, R. *et al.* Partitioning of small amphiphiles at surfactant bilayer/water interfaces: An avoided level crossing muon spin resonance study. *Langmuir* **20**, 2652-2659, doi:10.1021/la036188s (2004).
151 Veatch, S. L., Leung, S. S. W., Hancock, R. E. W. & Thewalt, J. L. Fluorescent probes alter miscibility phase boundaries in ternary vesicles. *J. Phys. Chem. B* **111**, 502-504, doi:10.1021/jp067636i (2007).
152 Hamley, I. W. *Introduction to Soft Matter: Synthetic and Biological Self-Assembling Materials, Revised Edition*. (John Wiley & Sons, Ltd, 2007).
153 Safinya, C. R., Sirota, E. B., Roux, D. & Smith, G. S. UNIVERSALITY IN INTERACTING MEMBRANES - THE EFFECT OF COSURFACTANTS ON THE INTERFACIAL RIGIDITY. *Physical Review Letters* **62**, 1134-1137, doi:10.1103/PhysRevLett.62.1134 (1989).
154 Roduner, E. Muons, soap, and drug delivery - an invitation to enter a new field of research. *Physica B-Condensed Matter* **326**, 19-24, doi:10.1016/s0921-4526(02)01568-5 (2003).
155 Kiefl, R. F. *et al.* 29Si Hyperfine Structure of Anomalous Muonium in Silicon: Proof of the Bond-Centered Model. *Physical Review Letters* **60**, 224-226, doi:10.1103/PhysRevLett.60.224 (1988).
156 Cox, S. F. J. *et al.* Experimental Confirmation of the Predicted Shallow Donor Hydrogen State in Zinc Oxide. *Physical Review Letters* **86**, 2601-2604, doi:10.1103/PhysRevLett.86.2601 (2001).
157 Hofmann, D. M. *et al.* Hydrogen: A Relevant Shallow Donor in Zinc Oxide. *Physical Review Letters* **88**, 045504, doi:10.1103/PhysRevLett.88.045504 (2002).
158 Vilão, R. C. *et al.* Muonium donor in rutile TiO2 and comparison with hydrogen. *Physical Review B* **92**, 081202, doi:10.1103/PhysRevB.92.081202 (2015).
159 Brant, A. T., Yang, S., Giles, N. C. & Halliburton, L. E. Hydrogen donors and Ti3+ ions in reduced TiO2 crystals. *Journal of Applied Physics* **110**, 053714, doi:10.1063/1.3630964 (2011).
160 Gorelkinskii, Y. V. in *Hydrogen in Semiconductors II* Vol. 61 *Semiconductors and Semimetals* (ed Norbert H. Nickel) Ch. 3, 25-77 (Academic Press, 1999).
161 Cox, S. F. J. Muonium as a model for interstitial hydrogen in the semiconducting and semimetallic elements. *Reports on Progress in Physics* **72**, 116501, doi:10.1088/0034-4885/72/11/116501 (2009).
162 Yokoyama, K., Lord, J. S., Miao, J., Murahari, P. & Drew, A. J. Photoexcited Muon Spin Spectroscopy: A New Method for Measuring Excess Carrier Lifetime in Bulk Silicon. *Physical Review Letters* **119**, 226601, doi:10.1103/PhysRevLett.119.226601 (2017).
163 Alberto, H. V. *et al.* Slow-muon study of quaternary solar-cell materials: Single layers and p-n junctions. *Physical Review Materials* **2**, 025402, doi:10.1103/PhysRevMaterials.2.025402 (2018).

164 Woerle, J., Prokscha, T., Hallén, A. & Grossner, U. Interaction of low-energy muons with defect profiles in proton-irradiated Si and 4H-SiC. *Physical Review B* **100**, 115202, doi:10.1103/PhysRevB.100.115202 (2019).
165 Jackson, T. J. *et al.* Depth-resolved profile of the magnetic field beneath the surface of a superconductor with a few nm resolution. *Physical Review Letters* **84**, 4958-4961, doi:10.1103/PhysRevLett.84.4958 (2000).
166 Suter, A. *et al.* Observation of nonexponential magnetic penetration profiles in the Meissner state: A manifestation of nonlocal effects in superconductors. *Physical Review B* **72**, 024506, doi:10.1103/PhysRevB.72.024506 (2005).
167 Kozhevnikov, V. *et al.* Nonlocal effect and dimensions of Cooper pairs measured by low-energy muons and polarized neutrons in type-I superconductors. *Physical Review B* **87**, 104508 doi:10.1103/PhysRevB.87.104508 (2013).
168 Stilp, E. *et al.* Controlling the near-surface superfluid density in underdoped YBa2Cu3O6+x by photo-illumination. *Scientific Reports* **4**, 6250, doi:10.1038/srep06250 (2014).
169 Kozhevnikov, V., Suter, A., Prokscha, T. & Van Haesendonck, C. Experimental Study of the Magnetic Field Distribution and Shape of Domains Near the Surface of a Type-I Superconductor in the Intermediate State. *J. Supercond. Nov. Magn* **33**, 3361 – 3376, doi:10.1007/s10948-020-05576-1 (2020).
170 Morenzoni, E. *et al.* The Meissner effect in a strongly underdoped cuprate above its critical temperature. *Nat. Commun.* **2**, 272, doi:10.1038/ncomms1273 (2011).
171 Di Bernardo, A. *et al.* Intrinsic Paramagnetic Meissner Effect Due to s-Wave Odd-Frequency Superconductivity. *Phys. Rev. X* **5**, 041021, doi:10.1103/PhysRevX.5.041021 (2015).
172 Flokstra, M. G. *et al.* Remotely induced magnetism in a normal metal using a superconducting spin-valve. *Nat. Phys.* **12**, 57-61, doi:10.1038/nphys3486 (2016).
173 Flokstra, M. G. *et al.* Observation of Anomalous Meissner Screening in Cu/Nb and Cu/Nb/Co Thin Films. *Physical Review Letters* **120**, 247001, doi:10.1103/PhysRevLett.120.247001 (2018).
174 Stewart, R. *et al.* Controlling the electromagnetic proximity effect by tuning the mixing between superconducting and ferromagnetic order. *Physical Review B* **100**, 020505(R), doi:10.1103/PhysRevB.100.020505 (2019).
175 Krieger, J. A. *et al.* Proximity-Induced Odd-Frequency Superconductivity in a Topological Insulator. *Physical Review Letters* **125**, 026802, doi:10.1103/PhysRevLett.125.026802 (2020).
176 Boris, A. V. *et al.* Dimensionality Control of Electronic Phase Transitions in Nickel-Oxide Superlattices. *Science* **332**, 937-940, doi:10.1126/science.1202647 (2011).
177 Suter, A. *et al.* Two-Dimensional Magnetic and Superconducting Phases in Metal-Insulator La2-xSrxCuO4 Superlattices Measured by Muon-Spin Rotation. *Physical Review Letters* **106**, 237003, doi:10.1103/PhysRevLett.106.237003 (2011).
178 Suter, A. *et al.* Superconductivity drives magnetism in delta-doped La2CuO4. *Physical Review B* **97**, 134522, doi:10.1103/PhysRevB.97.134522 (2018).
179 Stilp, E. *et al.* Magnetic phase diagram of low-doped La2-xSrxCuO4 thin films studied by low-energy muon-spin rotation. *Physical Review B* **88**, 064419, doi:10.1103/PhysRevB.88.064419 (2013).
180 Maurel, L. *et al.* Nature of antiferromagnetic order in epitaxially strained multiferroic SrMnO3 thin films. *Physical Review B* **92**, 024419, doi:10.1103/PhysRevB.92.024419 (2015).
181 Langenberg, E. *et al.* Controlling the Electrical and Magnetoelectric Properties of Epitaxially Strained Sr1-xBaxMnO3 Thin Films. *Adv. Mater. Interfaces* **4**, 1601040, doi:10.1002/admi.201601040 (2017).
182 Maurel, L. *et al.* Engineering the magnetic order in epitaxially strained Sr1-xBaxMnO3 perovskite thin films. *APL Mater.* **7**, 041117, doi:10.1063/1.5090824 (2019).
183 Dunsiger, S. R. *et al.* Spatially homogeneous ferromagnetism of (Ga, Mn)As. *Nat. Mater.* **9**, 299-303, doi:10.1038/nmat2715 (2010).

184 Monteiro, P. M. S. *et al.* Spatially Homogeneous Ferromagnetism below the Enhanced Curie Temperature in EuO1-x Thin Films. *Physical Review Letters* **110**, 217208, doi:10.1103/PhysRevLett.110.217208 (2013).
185 Saadaoui, H. *et al.* Intrinsic Ferromagnetism in the Diluted Magnetic Semiconductor Co:TiO2. *Physical Review Letters* **117**, 227202, doi:10.1103/PhysRevLett.117.227202 (2016).
186 Levchenko, K. *et al.* Evidence for the homogeneous ferromagnetic phase in (Ga, Mn) (Bi, As) epitaxial layers from muon spin relaxation spectroscopy. *Scientific Reports* **9**, 3394, doi:10.1038/s41598-019-40309-y (2019).
187 Drew, A. J. *et al.* Direct measurement of the electronic spin diffusion length in a fully functional organic spin valve by low-energy muon spin rotation. *Nat. Mater.* **8**, 109-114, doi:10.1038/nmat2333 (2009).
188 Al Ma'Mari, F. *et al.* Beating the Stoner criterion using molecular interfaces. *Nature* **524**, 69, doi:10.1038/nature14621 (2015).
189 Moorsom, T. *et al.* Reversible spin storage in metal oxide-fullerene heterojunctions. *Science Advances* **6**, aax1085, doi:10.1126/sciadv.aax1085 (2020).
190 Hofmann, A. *et al.* Depth-Dependent Spin Dynamics in Thin Films of TbPc2 Nanomagnets Explored by Low-Energy Implanted Muons. *ACS Nano* **6**, 8390-8396, doi:10.1021/nn3031673 (2012).
191 Kiefl, E. *et al.* Robust Magnetic Properties of a Sublimable Single-Molecule Magnet. *ACS Nano* **10**, 5663-5669, doi:10.1021/acsnano.6b01817 (2016).
192 Prokscha, T. *et al.* Depth dependence of the ionization energy of shallow hydrogen states in ZnO and CdS. *Physical Review B* **90**, 235303, doi:10.1103/PhysRevB.90.235303 (2014).
193 LEM. *LEM publication list*, <<Go to WoS>://WOS:000228050700106> (
194 Ponting, K. B. M. *The Metallurgy of Roman Silver Coinage: From the Reform of Nero to the Reform of Trajan*. (Cambridge University Press:, 2015).
195 Moreno-Suarez, A. I. *et al.* First attempt to obtain the bulk composition of ancient silver-copper coins by using XRF and GRT. *Nuclear Instruments & Methods in Physics Research Section B-Beam Interactions with Materials and Atoms* **358**, 93-97, doi:10.1016/j.nimb.2015.05.038 (2015).
196 Green, G. Understanding Roman Gold Coinage Inside Out. *In prep* (2020).
197 K. Ninomiya, M. K. K., T. Nagatomo, W. Higemoto, T. U. Ito, N. Kawamura, P. Strasser, K. Shimomura, Y. Miyake, T. Suzuki, Y. Kobayashi, S. Sakamoto, A. Shinohara, T. Sait. Nondestructive Elemental Depth-Profiling Analysis by Muonic X-ray Measurement. **87**, 4597-4600 (2015).
198 Clemenza, M. *et al.* CHNET-TANDEM experiment: Use of negative muons at RIKEN-RAL Port4 for elemental characterization of "Nuragic votive ship" samples. *Nuclear Instruments & Methods in Physics Research Section a-Accelerators Spectrometers Detectors and Associated Equipment* **936**, 27-28, doi:10.1016/j.nima.2018.11.076 (2019).
199 Kohler, E., Bergmann, R., Daniel, H., Ehrhart, P. & Hartmann, F. J. APPLICATION OF MUONIC X-RAY TECHNIQUES TO THE ELEMENTAL ANALYSIS OF ARCHAEOLOGICAL OBJECTS. *Nuclear Instruments & Methods in Physics Research* **187**, 563-568, doi:10.1016/0029-554x(81)90389-x (1981).
200 J Reidy, R. H., H Daniel, K. Springer. Use of Muonic X Rays for Nondestructive Analysis of Bulk Samples of Low Z Constituents. **50**, 40-44 (1978).
201 J. Reidy, R. H. K. S. USE OF MUONIC X RAYS FOR TISSUE ANALYSIS. *IEEE TAmuactionz on NbuCteak Science* **NS-22**, 1780-1783 (1975).
202 Hillier, A. D., Hampshire, B. V. & Ishida, K. in *Handbook of Cultural Heritage Analysis* (eds Sebastiano D'Amico & Valentina Venuti) (Springer, 2020).
203 Ziegler, J. F. & Lanford, W. A. EFFECT OF COSMIC-RAYS ON COMPUTER MEMORIES. *Science* **206**, 776-788, doi:10.1126/science.206.4420.776 (1979).

204 Sierawski, B. D. *et al.* Bias Dependence of Muon-Induced Single Event Upsets in 28 nm Static Random Access Memories. *2014 IEEE International Reliability Physics Symposium*, 2B.2.1-2B.2.5 (2014).
205 Sierawski, B. D. *et al.* Muon-Induced Single Event Upsets in Deep-Submicron Technology. *IEEE Trans. Nucl. Sci.* **57**, 3273-3278, doi:10.1109/tns.2010.2080689 (2010).
206 Mahara, T. *et al.* Irradiation Test of 65-nm Bulk SRAMs With DC Muon Beam at RCNP-MuSIC Facility. *IEEE Trans. Nucl. Sci.* **67**, 1555-1559, doi:10.1109/tns.2020.2972022 (2020).
207 Muonsources. *Muonsources*, <https://muonsources.org/> (
208 Tang, J. Y. *et al.* EMuS Muon Facility and Its Application in the Study of Magnetism. *Quantum Beam Science* **2**, doi:10.3390/qubs2040023 (2018).
209 Won, E. A Proposed Muon Facility in RAON/Korea. *JPS Conference Proceedings* **2**, 010110, doi:doi:10.7566/JPSCP.2.010110 10.7566/JPSCP.2.010110 (2014).
210 Williams, T. J. & MacDougall, P. G. J. Future Muon Source Possibilities at the SNS. (SNS, United States, 2017).
211 Jing, H. T., Meng, C., Tang, J. Y., Ye, B. J. & Sun, J. L. Production target and muon collection studies for an experimental muon source at CSNS. *Nuclear Instruments & Methods in Physics Research Section a-Accelerators Spectrometers Detectors and Associated Equipment* **684**, 109-116, doi:10.1016/j.nima.2012.05.045 (2012).
212 Pan, Z. W. *et al.* Conceptual design and update of the 128-channel mu SR prototype spectrometer based on musrSim. *JJAP Conference Proceedings* **7**, 011303, doi:10.1007/s41365-019-0648-5 (2019).
213 Kim, Y. J. Current status of experimental facilities at RAON. *Nuclear Instruments & Methods in Physics Research Section B-Beam Interactions with Materials and Atoms* **463**, 408-414, doi:10.1016/j.nimb.2019.04.041 (2020).
214 Liu, Y., Rakhman, A., Long, C. D. & Williams, T. J. Laser-assisted high-energy proton pulse extraction for feasibility study of co-located muon source at the SNS. *Nuclear Instruments & Methods in Physics Research Section a-Accelerators Spectrometers Detectors and Associated Equipment* **962**, 163706, doi:10.1016/j.nima.2020.163706 (2020).
215 PSI. *FLexible Advanced MuSR Environment (FLAME) Project*, <https://www.psi.ch/en/smus/flame-project> (
216 Hillier, A. D. *et al.* in *Proceedings of the 14th International Conference on Muon Spin Rotation, Relaxation and Resonance (?SR2017)* Vol. 21 *JPS Conference Proceedings* (Journal of the Physical Society of Japan, 2018).
217 Bonfà, P., Onuorah, I. J. & De Renzi, R. in *Proceedings of the 14th International Conference on Muon Spin Rotation, Relaxation and Resonance (?SR2017)* Vol. 21 *JPS Conference Proceedings* (Journal of the Physical Society of Japan, 2018).
218 Herak, M. *et al.* Magnetic order and low-energy excitations in the quasi-one-dimensional antiferromagnet CuSe${}_{2}$O${}_{5}$ with staggered fields. *Physical Review B* **87**, 104413, doi:10.1103/PhysRevB.87.104413 (2013).
219 Moller, J. S., Ceresoli, D., Lancaster, T., Marzari, N. & Blundell, S. J. Quantum states of muons in fluorides. *Physical Review B* **87**, 121108, doi:10.1103/PhysRevB.87.121108 (2013).
220 Bernardini, F., Bonfa, P., Massidda, S. & De Renzi, R. Ab initio strategy for muon site assignment in wide band gap fluorides. *Physical Review B* **87**, 115148, doi:10.1103/PhysRevB.87.115148 (2013).
221 Moller, J. S. *et al.* Playing quantum hide-and-seek with the muon: localizing muon stopping sites. *Physica Scripta* **88**, 068510, doi:10.1088/0031-8949/88/06/068510 (2013).
222 Bonfa, P. & De Renzi, R. Toward the Computational Prediction of Muon Sites and Interaction Parameters. *Journal of the Physical Society of Japan* **85**, 10, doi:10.7566/jpsj.85.091014 (2016).

223 Foronda, F. R. *et al.* Anisotropic Local Modification of Crystal Field Levels in Pr-Based Pyrochlores: A Muon-Induced Effect Modeled Using Density Functional Theory. *Physical Review Letters* **114**, 017602, doi:10.1103/PhysRevLett.114.017602 (2015).
224 Bonfa, P., Sartori, F. & De Renzi, R. Efficient and Reliable Strategy for Identifying Muon Sites Based on the Double Adiabatic Approximation. *J. Phys. Chem. C* **119**, 4278-4285, doi:10.1021/jp5125876 (2015).
225 Blundell, S. J. *et al.* mu SR study of magnetic order in the organic quasi-one-dimensional ferromagnet F4BImNN. *Physical Review B* **88**, 064423, doi:10.1103/PhysRevB.88.064423 (2013).
226 Huddart, B. M. *et al.* Magnetic order and enhanced exchange in the quasi-one-dimensional molecule-based antiferromagnet Cu(NO3)(2)(pyz)(3). *Physical Chemistry Chemical Physics* **21**, 1014-1018, doi:10.1039/c8cp07160h (2019).
227 Franke, K. J. A. *et al.* Magnetic phases of skyrmion-hosting GaV4S8-ySey (y=0, 2, 4, 8) probed with muon spectroscopy. *Physical Review B* **98**, 054428, doi:10.1103/PhysRevB.98.054428 (2018).
228 Onuorah, I. J., Bonfa, P. & De Renzi, R. Muon contact hyperfine field in metals: A DFT calculation. *Physical Review B* **97**, 174414, doi:10.1103/PhysRevB.97.174414 (2018).
229 Liborio, L., Sturniolo, S. & Jochym, D. Computational prediction of muon stopping sites using ab initio random structure searching (AIRSS). *Journal of Chemical Physics* **148**, 9, doi:10.1063/1.5024450 (2018).
230 Sturniolo, S. & Liborio, L. Computational prediction of muon stopping sites: A novel take on the unperturbed electrostatic potential method. *Journal of Chemical Physics* **153**, 10, doi:10.1063/5.0012381 (2020).